Reduced TBX5 dosage undermines developmental control of atrial cardiomyocyte identity in a model of human atrial disease

Irfan S. Kathiriya[1], Kavitha S. Rao[1,2], Alexander P. Clark[3], Kevin M. Hu[1,2,10], Zoe L. Grant[2], Megan N. Matthews[1], Zhe Chen[2], Jeffrey J. Saucerman[3,4], Swetansu K. Hota[2,11], Benoit G. Bruneau[2,5,6,7,8]

[1]Department of Anesthesia and Perioperative Care, University of California, San Francisco, USA, [2]Gladstone Institutes, USA, [3]Department of Biomedical Engineering, University of Virginia, USA;, [4]Robert M. Berne Cardiovascular Research Center, University of Virginia, USA;, [5]Roddenberry Center for Stem Cell Biology and Medicine, Gladstone Institutes, USA, [6]Cardiovascular Research Institute, University of California, San Francisco, USA, [7]Department of Pediatrics, University of California, San Francisco, [8]Institute of Human Genetics, University of California, San Francisco, 11 University of California, San Francisco [10]Current address: Creighton University School of Medicine, USA, [11]Current address: Herman B. Wells Center for Pediatric Research, Indiana University School of Medicine, USA

Correspondence to I.S.K irfan.kathiriya@ucsf.edu or B.G.B. benoit.bruneau@gladstone.ucsf.edu

Abstract

There is evidence for a shared genetic basis of atrial septal defects (ASDs) and atrial fibrillation (AF), but it remains unclear how genetic susceptibility leads to these distinct human atrial diseases. Here, we used directed differentiation of human induced pluripotent stem cell to ventricular or atrial cardiomyocytes (CMs) to define gene regulatory networks (GRNs) of human ventricular or atrial CM identity. In ventricular, atrial, or both types of CMs, we uncovered accessible chromatin regions, transcription factor motifs and key regulatory nodes, including the transcription factor *TBX5*, which is linked to ASDs and AF in humans. Complete *TBX5* loss resulted in a near absence of atrial CMs with a concomitant increase in abundance of other cell types. Reduced dosage of TBX5 in human atrial CMs caused cellular, electrophysiologic and molecular phenotypes consistent with features of atrial CM dysfunction. This included dose-dependent aberrant accessibility of many chromatin regions leading to perturbed TBX5-sensitive gene regulatory networks of atrial CM identity. These results suggest that genetic susceptibility to some human atrial diseases may impair developmental gene regulation for proper atrial CM identity.

35 **Introduction.**

36 Thin-walled atria are distinct from thick-walled ventricles in their developmental origin and
37 function. Atria serve to collect blood in the heart, initiate and propagate an electrical signal for
38 coordinated cardiac contraction, and respond to physiologic changes such as heart failure by
39 secreting hormones. These functions are reflected in atrial cell type abundance and phenotype.
40 For example, atrial fibroblasts display a greater response to pathologic stimuli than ventricular
41 fibroblasts (Burstein et al., 2008). Atrial cardiomyocytes (CMs) display distinct electrophysiologic
42 characteristics, calcium handling and contractile proteins, cell-cell coupling and energy
43 metabolism, which is reflected in human atrial gene expression *in vivo* (Dobrev et al., 2019).

44 Atrial disease is common and increases cardiovascular and cerebrovascular risk.
45 Developmental defects of the atria include cor triatriatum, atrial aneurysms, patent foramen ovale
46 (PFO) and atrial septal defects (ASDs). ASDs are one of the most common forms of congenital
47 heart defects (CHDs), estimated at 25% in the CHD population (Hoffman and Kaplan, 2002).
48 Some larger ASDs can lead to heart failure and require surgical repair. With aging, atrial tissue
49 can manifest with chaotic electrical activity, known as atrial fibrillation (AF). AF is the most
50 common arrhythmia and a leading cause of heart failure, stroke and sudden cardiac death (Kornej
51 et al., 2020). Moreover, there is an increasing prevalence of AF in adults with CHDs, and AF risk
52 is higher in patients with ASDs than in the non-CHD population (Miguel and Ávila, 2021).
53 Moreover, a molecular basis of ASDs and AF remains poorly understood, and critical insights are
54 needed to develop new diagnostic and therapeutic approaches.

55 There is ample evidence for a shared genetic basis of atrial diseases. ASDs are caused
56 by inherited dominant mutations in genes of the sarcomere (Ching et al., 2005; Matsson et al.,
57 2008; Postma et al., 2011), chromatin modifying enzymes (Boniel et al., 2021) and transcription
58 factors (Basson et al., 1997; Garg et al., 2003; Kirk et al., 2007; Li et al., 1997; Posch et al., 2010;
59 Schott et al., 1998; Yuan et al., 2013). Atrial fibrillation is associated with inherited mutations or
60 variants in genes of potassium channels (Chen et al., 2003; Hong et al., 2005; Olson et al., 2006;
61 Xia et al., 2005; Yang et al., 2004), the sarcomere (Choi et al., 2018; Gudbjartsson et al., 2016;
62 Lee et al., 2018), atrial natriuretic peptide (Hodgson-Zingman et al., 2008) and transcription
63 factors (Guo et al., 2016; Ma et al., 2016; Roselli et al., 2018; Xie et al., 2013). Thus, some
64 categories of genes associated with ASDs and AF share functional overlap, but the mechanisms
65 underlying or linking the two atrial diseases are unclear.

66 To model human atrial disease *in vitro*, multiple groups have developed methods to
67 promote atrial CM differentiation of human pluripotent stem cells, garnering important insights into
68 the pathways involved (Cyganek et al., 2018; Lee et al., 2017; Zhang et al., 2019). These

69 protocols have been used in wildtype cells for cell type-specific drug screening, and for inducing
70 AF by electrical stimulation (Goldfracht et al., 2019) or with drugs that increase the risk of AF
71 (Shafaattalab et al., 2019). However, human cellular models of genetic susceptibility to atrial
72 disease have not yet been reported.

73 Heterozygous mutations of the transcription factor *TBX5* cause Holt-Oram syndrome, a
74 developmental disorder that often includes ASDs in humans (Basson 1997,Li 1997) and in mice
75 (Bruneau et al., 2001). Conditional loss of *Tbx5* in the endocardium (Nadeau et al., 2010) or dorsal
76 mesenchymal protrusion (Xie et al., 2012) leads to ASDs, suggesting an essential role for TBX5
77 in atrial septal development. Post-natal deletion of *Tbx5* in atrial CMs leads to AF via a calcium
78 transport mechanism (Dai et al., 2019; Nadadur et al., 2016), and *Tbx5* was shown to be essential
79 for the maintenance of an atrial gene expression program (Sweat et al., 2023). Some inherited
80 *TBX5* mutations cause both ASDs and AF in the same individuals (Bever et al., 1996; Postma et
81 al., 2008). As TBX5 is broadly associated with atrial gene regulation, ASDs and AF, understanding
82 TBX5 function presents an opportunity to decipher generalizable rules of gene regulation from
83 atrial development and disease.

84 Here, we deployed a recently developed induced pluripotent stem cell (iPSC) model of
85 Holt-Oram Syndrome (Kathiriya et al., 2021) to study genetic susceptibility to human atrial
86 diseases. We observed disease-relevant cellular, electrophysiologic and molecular deficits of
87 atrial CMs. Many deficits showed more profound disturbances to cell physiology and
88 developmental gene expression than in ventricular CMs (Kathiriya et al., 2021). Notably, atrial CM
89 specification failed from complete loss of *TBX5,* and atrial CM identity was hindered by
90 heterozygous loss of *TBX5*. Further, we discovered gene regulatory networks (GRNs) for atrial
91 CM identity that were sensitive to reduced or absent TBX5 dosage, and we defined disruptions to
92 key nodes, including ASD- and AF-risk genes, in atrial disease-relevant networks.
93

94 **Results**.

95 <u>Modeling chamber-specific atrial CM identity from human iPSCs.</u> As an initial step to model atrial
96 differentiation and disease, we used two distinct protocols to differentiate wildtype (WT) iPSCs
97 (WTC11 parental line) (Miyaoka et al., 2014) to either atrial or ventricular CMs to validate atrial
98 CM-specific characteristics compared to ventricular CMs. Immunostaining showed ANP, a well-
99 known atrial marker, to be enriched in atrial CMs (Fig. 1A-G). By contrast, MLC2V, a ventricular
100 marker, was nearly absent among atrial CMs compared to ventricular CMs (Fig. 1H-N).
101 Multielectrode array (MEA) assays revealed a faster beat rate among atrial CMs and shorter rate-
102 adjusted local extracellular action potentials (LEAP), consistent with atrial CM electrophysiology

103 (Fig. 1O, P)(Nerbonne and Kass, 2005), consistent with iPSC-derived atrial CMs derived by
104 another protocol (Cyganek et al., 2018).
105 We performed single cell RNA sequencing (scRNA seq) on atrial differentiation at day 20
106 and merged it with previously generated scRNA seq data of ventricular differentiation at day 23
107 (Fig. S1A, B) (Kathiriya et al., 2021). Differential expression analysis confirmed that atrial CMs
108 were enriched for genes including *TBX5* and *NPPA*, along with other atrial-specific genes
109 (*NR2F2, HEY1, HAMP, MYH6*), while devoid of ventricular-specific genes (*MYL2*, *IRX4, HEY2,*
110 *HAND1, MYH7*) (Fig. 1Q) (Supp. Data 1).
111
112 Distinct epigenomic features in human iPSC-derived atrial CMs. We next compared accessible
113 chromatin regions among differentiations to ventricular or atrial CMs using single nucleus ATAC
114 sequencing (snATAC seq) (Fig. S1C, D, Supp. Data 2). We annotated cell type clusters by ArchR
115 gene score (Granja et al., 2020), and defined *MYL2*-gene score$^+$ clusters as ventricular CMs and
116 *MYH6*-gene score$^+$ clusters as atrial CMs (Fig. S1E). In a *TNNT2*-gene score$^+$ CM subset of
117 ventricular and atrial CMs (Fig. S1F, G), we found that accessible chromatin regions among
118 clusters of ventricular or atrial CMs were distributed across promoters, introns, exons and distal
119 regions to a similar degree (Fig. S1H). By genomic coordinates, about one-quarter of accessible
120 regions (42,108 regions) overlapped between ventricular and atrial CMs at the stages assessed.
121 Likewise, 56,301 ventricular CM-specific and 63,173 atrial CM-specific regions were identified
122 (Fig. 1R). Based on fold change differences, we also identified 465 differentially accessible
123 regions (DAR) among ventricular or atrial CMs (Fig. S1I). Thus, although several accessible
124 regions may be common to ventricular and atrial CMs, the degree of accessibility may be different
125 among ventricular or atrial CMs. Among DARs, transcription factor (TF) motifs enriched among
126 ventricular CMs included MADS-box/MEF2 (Desjardins and Naya, 2016; Medrano and Naya,
127 2017; Naya et al., 2002), TEAD (Gise et al., 2012; Lin et al., 2016) and NFAT (Bushdid et al.,
128 2003) motifs (Fig. 1S). Interestingly, HOX motifs were also enriched in iPSC-derived ventricular
129 CMs, implying a HOX factor may have potential as an important regulatory TF during human
130 ventricular development. Atrial CMs were enriched for NKX, NR2F2, GATA and TBX/MEIS motifs
131 (Fig. 1S). Notably, TF motifs of TGIF, a TALE homeodomain protein associated with
132 holoprosencephaly that inhibits retinoic acid signaling (Bartholin et al., 2006) and represses Smad
133 signaling (Nakashima et al., 2018) were observed. However, a role for TGIF or TGIF-like factors
134 in atrial development has not yet been described.
135

136 Gene regulatory networks of atrial cardiomyocyte (CM) identity. Gene regulatory networks
137 (GRNs) can reveal nodes—TFs that are important for establishment and maintenance of
138 transcriptional programs—beyond changes to gene expression. To uncover GRNs of human
139 ventricular or atrial CM identity, we applied CellOracle, a machine learning-based approach to
140 build cell type-specific GRNs using both gene expression and chromatin accessibility data (Supp.
141 Data 3) (Kamimoto et al., 2023). We calculated metrics of 'betweenness" (i.e., metric of
142 information flow through each node) and 'degree out' (i.e., count of outgoing edge each node)
143 centrality of each node (Fig. S1J, K). We observed that canonical TFs such as *HEY2*, *HAND1*,
144 *HES4* as predominant nodes in ventricular CMs, and *NR2F2* and *HEY1* in atrial CMs. We also
145 identified TFs that are lesser known in the developing heart as nodes, including *E2F1* in
146 ventricular CMs and *NR2F1* and *PLAGL1* in atrial CMs. Of note, some TFs (e.g. *HEY2*, *HEY1*,
147 *TBX5*) displayed connections in both ventricular and atrial CM GRNs, although the nature of their
148 connections changed, reflecting ventricular or atrial CM contexts (Fig. 1T, U). For example,
149 ventricular-enriched *HEY2* displayed predominant betweenness centrality and degree out in
150 ventricular CMs (Fig. S1J, K). In ventricular CMs, ventricular-enriched *HEY2* displayed
151 connections with a positive correlation (i.e. directly proportional between the TF and a target gene
152 known as an edge), suggesting that *HEY2* positively regulates some ventricular CM genes. Some
153 atrial CM-specific connections of *HEY2* reflected negative correlations (i.e. inversely proportional
154 between the TF and an edge), suggesting *HEY2* may negatively regulate some atrial CM genes
155 (Fig. S1L, M). Notably, atrial-enriched *HEY1* displayed predominant betweenness centrality and
156 enriched degree out in atrial CMs (Fig. S1J, K). Interestingly, atrial-enriched *HEY1* showed most
157 connections reflecting positive correlations in ventricular CMs, while many connections in atrial
158 CMs reflected negative correlations, suggesting that the relationship of *HEY1* to gene expression
159 is more complex in the atrial CM context (Fig. S1N, O). Notably, although there are more direct
160 connections to *TBX5* in ventricular CMs, *TBX5* showed connections with positive correlations in
161 both atrial and ventricular CMs, some of which were overlapping, implying some shared roles in
162 both ventricular and atrial CM networks (Fig. 1V, W).
163 As variants in *TBX5* are associated with ASDs and AF, we predicted that *TBX5* likely plays
164 a central regulatory role in human atrial CMs. We used CellOracle (Kamimoto et al., 2023) to
165 perform *in silico* perturbation of *TBX5* in atrial CM differentiation. In the normal condition, WTC11
166 cells generate mostly *MYH6*$^{+}$ atrial CMs, some *MYH7*$^{+}$ ventricular-like CMs and *TNNT2*$^{+}$
167 *COL3A1*$^{+}$ CMs, which express extracellular matrix genes (CMEs). CellOracle analysis predicted
168 that complete loss of *TBX5* would hinder specification of atrial CM identity and instead lead toward
169 other CM sub-types, such as CMEs (Fig. 1X, Y).

170

171 Human cell model of genetic susceptibility to atrial diseases. To test this prediction, we leveraged
172 a human disease model of *TBX5* haploinsufficiency (Kathiriya et al., 2021) to study genetic
173 susceptibility to atrial diseases. We deployed a commercial protocol (StemCell Technologies) for
174 atrial CM differentiation of iPSCs with heterozygous (*TBX5*$^{in/+}$) or homozygous (*TBX5*$^{in/del}$) *TBX5*
175 loss of function (LOF) mutation, or their wild-type parental line (WTC11) (Kathiriya et al., 2021).
176 Western blot confirmed reduced levels of TBX5 in *TBX5*$^{in/+}$ cells and absence of TBX5 in *TBX5*$^{in/del}$
177 cells at day 20 of atrial CM differentiation (Fig. S2A, B). While *TBX5*$^{in/+}$ cells differentiated to
178 beating atrial CMs, *TBX5*$^{in/del}$ cells often had compromised CM differentiation efficiency and rarely
179 produced beating CMs (Fig. 2A). Further, *TBX5*$^{in/del}$ atrial CMs could not be recovered beyond
180 day 20, indicating a more severe phenotype than homozygous *TBX5* mutant ventricular CMs
181 (Kathiriya et al., 2021).
182 Dosage-sensitive sarcomere disarray and increased cell size were observed in both
183 *TBX5*$^{in/del}$ and *TBX5*$^{in/+}$ atrial CMs at day 20 of differentiation (Fig. 2B-F), indicating atrial CM
184 dysfunction. Notably, increased cell size in *TBX5*$^{in/+}$ atrial CMs was not observed previously in
185 *TBX5*$^{in/+}$ ventricular CMs (Kathiriya et al., 2021), suggesting that some cellular phenotypes are
186 more susceptible to reduced TBX5 dosage in atrial CMs. Upon replating *TBX5*$^{in/+}$ cells for micro-
187 electrode array (MEA), we observed a prolonged local extracellular action potentials (LEAPs) with
188 a broader plateau phase (Fig. 2G-J), reminiscent of ventricular-like CMs. This prolonged action
189 potential was consistent with observations from mouse *Tbx5*$^{-/-}$ atrial CMs (Yang et al., 2017) and
190 human *TBX5* heterozygous mutant ventricular CMs (Bersell et al., 2023; Kathiriya et al., 2021),
191 albeit using different methods.
192

193 Disrupted specification of atrial CMs from complete loss of *TBX5*. To determine the gene
194 expression changes that underlie these functional differences in *TBX5*-deficient atrial CMs, we
195 performed scRNA-seq on these cells at day 20 of atrial CM differentiation (Supp. Data 4). A high-
196 level annotation of cell type clusters included *TNNT2*$^{+}$ CMs (WT 60.6% *TNNT2*, *TBX5*$^{in/+}$ 59% and
197 *TBX5*$^{in/del}$ 0.4%), *DLK1*$^{+}$ or *DCN*$^{+}$ fibroblast-like cells, *EPCAM*$^{+}$ epithelial-like cells, *SERPINA1*$^{+}$ or
198 *TTR*$^{+}$ endodermal population, *TOP2A*$^{+}$ dividing cells and *NEFM*$^{+}$ neural-like cells (Fig. 2K-M).
199 Using a generalized linear mixed effects model, we tested genotype-specific differences in cluster
200 memberships. Indeed, *TBX5*$^{in/del}$ cells were significantly enriched in non-CM clusters of fibroblasts
201 and epithelial-like cells, with a concomitant loss of CMs (Fig. 2N, S2C). As cluster assignments
202 can change with UMAP resolution, we also employed Milo, a program that tests differential
203 abundance by assigning cells to partially overlapping neighborhoods on a k-nearest neighbor

204 graph (Dann et al., 2022). This method also showed a statistically significant change in the
205 abundance of CMs, fibroblasts, epithelial and neural-like cells for *TBX5*$^{in/del}$ (Fig. 2O, P). In
206 contrast, cell type abundance among *TBX5*$^{in/+}$ cells was generally similar to WT at this resolution.
207
208 <u>TBX5-sensitive perturbations to atrial CM identity.</u>
209 Next, we evaluated *TNNT2*$^{+}$ clusters and defined CM subtypes (Fig. 3A-C). In WT CMs,
210 we identified CM subtypes that were enriched for *MYH6*$^{+}$ expression, such as *PITX2*$^{+}$ left atrial
211 (LA)-like CMs, *HAMP*$^{+}$ right atrial (RA)-like CMs, *NPPA*$^{+}$ CMs, *RSPO3*$^{+}$ atrioventricular (AV) CMs
212 and a cluster lacking expression of LA- or RA-like markers, which we inferred as atrial precursor-
213 like CMs by pseudotime analysis with Monocle 3 (Cao et al., 2019) (Fig. 3D). Other clusters that
214 had relatively lower *MYH6*$^{+}$ expression included *MYH7*$^{+}$ ventricular-like CMs expressing
215 ventricular-enriched genes (e.g. *IRX4, HEY2*), *COL3A1*$^{+}$ clusters expressing fibroblast genes
216 (e.g. *COL1A1*, *FN*, *SOX4*, *TGFB2*), resembling CMs expressing extracellular matrix genes
217 (CMEs) in developing mouse hearts (DeLaughter et al., 2016). We also observed a small *HBD*$^{+}$
218 hematopoietic-like cluster.
219 While similar numbers of total *TNNT2*$^{+}$ CMs were observed for WTC11 (9823 cells) and
220 *TBX5*$^{in/+}$ (9311 cells), only 59 *TNNT2*$^{+}$ CMs were observed in *TBX5*$^{in/del}$, indicating severely
221 impaired atrial CM differentiation. *TBX5*$^{in/del}$ CMs were devoid of *NPPA*$^{+}$ CMs and RA-like CMs
222 but were observed in CME and AV CM clusters. Further, only two atrial precursor-like CMs were
223 observed in *TBX5*$^{in/del}$, indicating an absence of proper atrial CM specification, consistent with *in*
224 *silico* predictions (Fig. 1X, Y).
225 Although *TBX5*$^{in/+}$ cells were among RA-like, LA-like and *NPPA*$^{+}$ CM clusters, *TBX5*$^{in/+}$
226 cells were significantly reduced in numbers, implicating a deficiency of proper atrial CM identity
227 (Fig. 3E). Concomitantly, *TBX5*$^{in/+}$ cells were significantly enriched for CMEs and AV CMs. These
228 observations imply a spectrum of phenotypes from *TBX5* heterozygous mutant cells, with some
229 *TBX5* heterozygous mutant cells remaining similar to WT cells, while others were found in a *TBX5*
230 heterozygous-predominant cluster (e.g. CME-1) (Fig. S3A). Such variability in cellular phenotypes
231 may be of interest, as many affected members of multi-generational families of Holt-Oram
232 Syndrome, and genetically-determined CHDs in general, express variations in cardiac
233 phenotypes (Basson et al., 1994; Benson et al., 1998; Benson et al., 2003; Garg et al., 2003;
234 Garg et al., 2005).
235
236 <u>ASD- and AF-risk genes are vulnerable to reduced TBX5 dosage.</u> Complete loss of *TBX5* in atrial
237 CMs led to reduced expression of 243 genes and increased expression of 340 genes (Fig. 3E,

238 Supp. Data 4). Heterozygous loss of *TBX5* resulted in reduced expression of 283 genes and
239 increased expression of 279 genes (Fig. 3F). Differentially expressed genes were significantly
240 enriched for known AF-, ASD-, or CHD-risk or causative genes (Fig. 3H-I, Supp. Data 5). In *TBX5*
241 heterozygous mutant cells, susceptible genes included 8 ASD- (e.g. *TBX20, FGFR2, GLI3,*
242 *KAT6B, PBX1*), 80 AF (e.g. *DES, CAMK2D, ID1, VCAM1*) and 4 ASD and AF- (e.g. *PITX2,*
243 *ACTC1, MYH7*) risk genes (Fig. 3K). Further, dose-dependent genes dysregulated in both *TBX5*
244 mutant genotypes included atrial-specific genes (e.g. *NR2F2*, *HEY1*, *HAMP*), sarcomere genes
245 (e.g. *TNNC1*, *TNNT2*), ECM genes (e.g. *COL3A1*, *FN1*) and AV canal markers (e.g. *RSPO3*,
246 *BMP2*). Many genes could be further categorized as risk genes for ASDs (e.g. *NR2F2, JAG1*)
247 (Ching et al., 2005; McElhinney et al., 2002; Turki et al., 2014), AF (e.g. *NPPA*, *TECRL, TTN)*
248 (Choi et al., 2018; Devalla et al., 2016; Hodgson-Zingman et al., 2008; Lee et al., 2018), or both
249 ASDs and AF (e.g. *MYH6*) (Ching et al., 2005; Lee et al., 2018; Postma et al., 2008; Postma et
250 al., 2011; Roselli et al., 2018; Vad et al., 2020; Yuan et al., 2013).
251 Many previously characterized TBX5 targets (e.g. *NPPA*, *MYH6, PITX2, DES*) (Bruneau
252 et al., 2001; Garg et al., 2003; Kathiriya et al., 2021; Ouwerkerk et al., 2021) displayed TBX5
253 dose-dependent dysregulation. We also discovered new putative TBX5 downstream genes,
254 genes such as *ANGPT1, NR2F1* and *MEG3* (Fig. 3E-L). Notably, *ANGPT1*, with known roles in
255 cardiac jelly homeostasis during atrial chamber morphogenesis (Kim et al., 2018), was
256 downregulated in *TBX5* mutant CMs, whereas *MEG3*, a positive regulator of cardiac fibrosis
257 (Piccoli et al., 2017) was downregulated in $TBX5^{in/+}$ and upregulated in $TBX5^{in/del}$ CMs. We
258 confirmed altered mRNA expression of *NR2F1, DES*, *ANGPT1* and *MEG3* in *TBX5* mutant atrial
259 CMs by fluorescent *in situ* hybridization (Fig. 4 A-M).
260 To determine if disturbances to atrial CM identity from reduced TBX5 are exacerbated
261 later in atrial CM differentiation, we performed scRNA-seq at a later time point, at day 45, of
262 $TBX5^{in/+}$ atrial cells. Although both high level-cell type annotations as well as CM subtypes at day
263 45 were similar to those observed at day 20, fewer $TNNT2^{+}$ CMs and more $POSTN^{+}$ fibroblasts
264 were observed among $TBX5^{in/+}$ at day 45 (Fig. S4A-D). Among CM sub-types at day 45, $HAMP^{+}$
265 RA-like, and $PITX2^{+}$ LA-like CMs were reduced, while CME-2s and $MYH7^{+}$ ventricular-like CMs
266 were enriched (Fig. S4E-H). These results indicated that $TBX5^{in/+}$ cells failed to differentiate to
267 RA- and LA-like atrial CMs with a deviation towards CMEs and ventricular-like CMs, similar to
268 $TBX5^{in/del}$ at day 20 and analogous to the *in silico* predictions. At day 45, 244 differentially
269 expressed genes were upregulated and 144 genes were downregulated in $TBX5^{in/+}$ CMs (Fig.
270 S4I). These included 6 ASD- , 72 AF, and 5 ASD and AF- risk genes (Fig. S4J). A significant
271 overlap with CHD- and AF-risk genes at day 45 were observed (Fig. S5A, B), including 3 ASD-

272 (e.g. *NR2F2, GPC3, MEIS2*), 17 AF- (e.g. *ANGPT1, NPPA, TNNT2, TNNI3*) and 2 ASD and AF-
273 (e.g. *MYH7, ACTC1*) risk genes (Fig. S5C-E).
274
275 Dosage-sensitive perturbations to chromatin accessibility in atrial CMs. To evaluate the degree
276 to which altered chromatin accessibility could help explain disturbances to gene expression by
277 reduced TBX5 dosage in atrial CMs, we performed single nucleus (sn) ATAC-seq analysis of WT
278 and *TBX5* mutant cells at day 20 of atrial CM differentiation (Fig. 5A, B, Fig. S6A, Supp. Data 6).
279 Among *TNNT2* gene score^{+} clusters, cluster C5 was enriched for *TBX5*$^{in/del}$ cells, which showed
280 reduced gene scores for *MYH6*, *PITX2, HAMP* and *NPPA,* and increased gene scores for
281 *COL3A1*, indicating disrupted chromatin accessibility of CMs from complete *TBX5* loss. In
282 contrast, cluster C6 was enriched for *TBX5*$^{in/+}$ cells and displayed reduced gene scores for *PITX2*,
283 *HAMP* and *NPPA*, consistent with disturbed chromatin accessibility of atrial CMs from
284 heterozygous loss of *TBX5* (Fig. 5C, D, Fig. S6B).
285 We analyzed differentially accessible regions (DARs) from reduced TBX5 dosage for TF
286 motif loss or enrichment. Among *TBX5*$^{in/del}$, we found a loss of atrial-enriched NKX, TBX/MEIS
287 and TFIG motifs between WT-enriched and *TBX5*$^{in/del}$-enriched clusters. Similarly, in *TBX5*$^{in/+}$, we
288 observed a loss of NKX, TBX/MEIS, GATA, NR2F2 and TGIF between WT-enriched and *TBX5*$^{in/+}$-
289 enriched clusters (Fig. 5E, F, S6C-E). These TF motifs suggested a broadly disturbed deployment
290 of cardiac TFs for atrial CM identity in *TBX5* mutants. In contrast, TF motifs gained in in *TBX5*$^{in/del}$
291 atrial CMs included non-heart associated NFIA, NFIB, NFIX, right ventricular and outflow tract-
292 associated HAND, and BMP-responsive SMAD motifs (Fig. 5E, F). In *TBX5*$^{in/+}$, motifs for the
293 epicardial-associated WT1 were gained (Fig. 5E, F). These changes to TF motifs suggested
294 gained accessibility by non-atrial CM TFs, consistent with ectopic expression of non-atrial CM
295 genes.
296 As TBX and MEIS motifs share sequence similarity, we evaluated DARs with predicted
297 TBX/MEIS motifs. We observed that approximately 40% of regions less accessible in *TBX5*
298 mutant CMs contained TBX/MEIS motifs compared to about 20% of regions more accessible in
299 *TBX5* mutant CMs (Fig. 5G). Further, in *TBX5* mutants, we overlaid TBX5 occupancy in WT cells
300 (Grant et al., 2025) and found that 40-60% of less accessible regions overlapped with TBX5
301 binding, compared to 5% or less of more accessible regions (Fig. 56G'), suggesting that proper
302 TBX5 dosage was essential for open chromatin in atrial CMs, rather than closed chromatin.
303 Evaluation of chromatin accessibility near differentially-expressed genes showed correlations
304 between gene expression and chromatin accessibility (Fig S6F-K). Some examples of DARs
305 across genotype-enriched clusters included the proximal promoter of the AF-linked gene *NPPA*

306 (Horsthuis et al., 2008), the nearby *NPPA-NPPB* super enhancer (Man et al., 2021) (Fig. 5H), as
307 well as at the promoter of the novel TBX5-dependent atrial CM target *NR2F1* (Fig. 5I).
308
309 Network disruptions to disease-related connections in atrial CMs from reduced TBX5 dosage. We
310 used CellOracle (Kamimoto et al., 2023) to infer GRNs of atrial CMs by *TBX5* genotype and to
311 understand how reduced TBX5 dosage perturbs network connections for human atrial CM identity
312 (Fig. 6, Supp. Data 7). We observed a reduced number of total nodes with decreasing TBX5
313 dosage (1106 in WT; 1028 in *TBX5*$^{in/}$; 941 in *TBX5*$^{in/del}$) (Fig. S7A), with a concomitant increase
314 in condition-specific edges (i.e., those present only in one condition and absent in the others) (900
315 in WT, 1436 in *TBX5*$^{in/+}$, 1625 in *TBX5*$^{in/del}$) (Fig. S7B). Many network connections displayed shifts
316 from positive correlations (i.e. directly proportional changes between TF and edge) to negative
317 correlations (i.e. inversely proportional between TF and edge) (e.g. *NR2F1*, *NKX2-5*, *HEY1,*
318 *TCF21*) (Fig. 6A-C, Fig. S7C-F). Furthermore, a network comprised of TF sources to TBX5 (i.e.
319 upstream TFs connected to TBX5) or CHD-, ASD- and AF-risk TFs susceptible to reduced TBX5
320 dosage showed fewer unique edges (61 in WT, 47 in *TBX5*$^{in/+}$*,* 36 in *TBX5*$^{in/del}$) and total nodes
321 (27 in WT, 25 in *TBX5*$^{in/+}$*,* 19 in *TBX5*$^{in/del}$) (e.g. ASD-risk *SMC3* lost in *TBX5*$^{in/+}$ and *TBX5*$^{in/del}$,
322 *MEF2A* lost in *TBX5*$^{in/+}$) (Fig. 6D-F). These results indicated that these networks are less complex
323 when TBX5 dosage is reduced, implying a loss to a TBX5-dependent atrial CM program.
324 Moreover, centrality of selected TFs were sensitive to reduced *TBX5*. *TBX5* showed an
325 absence of significant network connections in *TBX5*$^{in/+}$ and *TBX5*$^{in/del}$ by betweenness or degree
326 out centrality (Fig. 6G, H). This included loss of all 25 connections, including with the highest
327 correlated gene *PGAM1*, along with *BMP5,* AF-risk *NPPA*, and ASD- and AF-risk *MYH7* (Fig. 6I),
328 consistent with profound disturbances to *TBX5* connections, even from disease-associated
329 heterozygous loss of *TBX5* in atrial CMs.
330 Several TFs showed consistency of betweenness and degree out centrality (e.g.
331 ventricular-enriched *E2F1*, atrial-enriched *PLAGL1*, fibroblast-enriched *TCF12*), while other TFs
332 showed discordance between centrality metrics (e.g. *NR2F1, TCF21*) (Fig. 6G, H). For example,
333 *NR2F1* showed a dosage-sensitive step-wise decrease in betweenness centrality with a complete
334 loss in *TBX5*$^{in/del}$ (Fig. 6G). In contrast, degree out of *NR2F1* was generally maintained in *TBX5*$^{in/+}$
335 and completely lost in *TBX5*$^{in/del}$ (Figure 6H, J). Although the number of degree out connections
336 of *NR2F1* in *TBX5*$^{in/+}$ was somewhat maintained, the strength of correlations, but not direction of
337 correlations, were altered in *TBX5*$^{in/+}$ (e.g. AF-risk *ANGPT1*, *MYL7, ASD-risk NR2F2, SELENOP*)
338 (Fig. 6J). Some *NR2F1* connections were lost (e.g. *NDUFB9*, *NDUFS7, ETFA, ARHGAP5,*
339 *CDC42EP3*) or gained (e.g. *NES*, *PPP1R12B, KDELR, APOA1, CNN3*), consistent with a

340 reconfiguration of *NR2F1* connections in response to reduced TBX5. In contrast, betweenness
341 centrality of fibroblast-associated *TCF21* was not apparent in all three *TBX5* genotypes (Fig. 6G),
342 suggesting that *TCF21* may not be part of the core CM network. However, the few *TCF21*
343 connections by degree out in WTC11 were dramatically increased in $TBX5^{in/+}$ and $TBX5^{in/del}$ (Fig.
344 S7E), suggesting that abnormal connections of *TCF21* may reflect an ectopic fibroblast-like
345 network in *TBX5* mutants, potentially in conjunction with an increase in degree out connections
346 of the fibroblast-associated *TCF12* (Fig. S7F). In sum, we found that reduced TBX5 dosage
347 results in a reconfiguration of atrial CM networks, including disruptions to connections of ASD-
348 and AF-risk genes.
349
350 **DISCUSSION**.
351 This study describes a human cellular model of TBX5-associated atrial disease and
352 reveals dosage-sensitive disruptions to atrial CM GRNs. Our findings uncover vulnerabilities in
353 atrial CM identity and provide further evidence for a shared molecular basis of ASDs and AF.
354 These insights advance our understanding of genetic susceptibility to atrial diseases and provide
355 new potential avenues for therapeutic development.
356 Using human differentiation systems to CMs, we discern epigenetic differences between
357 two closely related cell types, ventricular and atrial CMs. These results provide further support
358 that these approaches may be useful to model cardiac diseases *in vitro* that affect one cell type
359 versus the other. For example, iPSC-derived ventricular CMs have been valuable to model
360 susceptibility to ventricular-specific diseases, such as hypertrophic or dilated cardiomyopathy,
361 ventricular arrhythmias, or congenital heart defect networks (Briganti et al., 2020; Friedman et al.,
362 2024; Hinson et al., 2015; Hnatiuk et al., 2021; Kathiriya et al., 2021; Knollmann, 2013; Lan et al.,
363 2013; Seeger et al., 2019; Sinnecker et al., 2013; Smith et al., 2018; Sun et al., 2012). Whereas
364 atrial CMs are distinct, human iPSC-derived atrial CMs can be leveraged for disease modeling of
365 AF, ASDs or other atrial diseases, to uncover atrial-relevant disturbances to GRNs and cellular
366 physiology. Likewise, human cellular models of atrial disease could be used for drug screening
367 for therapeutic potential, teratogenicity or atrial arrhythmia risk.
368 From our data, modeling GRNs of atrial or ventricular CM identity predicted key nodes
369 that could be critical for disrupting atrial GRNs. One of these key nodes is *TBX5*, which we and
370 others have studied (Bersell et al., 2023; Karakikes et al., 2017; Kathiriya et al., 2021). Here, we
371 have modeled reduced dosage, including absolute deficiency of *TBX5 in silico* and *in vitro*, in
372 human atrial cells. Based on changes in gene expression and chromatin accessibility, we have
373 inferred exquisitely sensitive GRNs that are important for atrial function and identity. It is

374 particularly striking that direct connections of multiple key nodes, such as *NR2F1* and ASD-risk
375 *NR2F2*, are affected within these dosage-vulnerable networks even from partial loss of *TBX5*,
376 leading to a cascading effect on susceptible downstream genes related to atrial CM identity.
377 Conversely, the gain of connections of fibroblast-associated *TCF21* and *TCF12* may reflect a
378 change in CM cell identity to CMEs, which express some fibroblast-like genes. In the setting of
379 genetic susceptibility to AF, for example, this perturbation of cell identity may contribute to an
380 atrial fibrosis-like state associated with AF (Platonov, 2017). Some of these nodes are genetically
381 associated with AF and/or ASDs, indicating that a broad disease network may underly their
382 pathologies.

383 The disrupted networks point to new TBX5-sensitive candidate genes, such as *NR2F1*,
384 *ANGPT1* and *MEG3*, and their biological processes as possible leads for therapeutic potential.
385 Moreover, targeting to revert perturbed dosage-sensitive GRNs may offer therapeutic
386 opportunities to restore proper atrial identity in patients with genetic or acquired atrial conditions,
387 as demonstrated in another cardiovascular disease context (Theodoris et al., 2020). By combining
388 computational modeling with analysis of this cellular disease model, predictions to enhance TBX5
389 activity or improve disturbed atrial GRNs could be tested to mitigate atrial disease susceptibility
390 by small molecules or gene editing.

391 In conclusion, our discovery of a broad disruption to the GRNs underlying atrial identity in
392 the setting of genetic susceptibility suggests that some atrial diseases, such as ASDs or AF, may
393 not only arise from disturbances of certain functional proteins, such as ion channels or
394 extracellular matrix components. Rather, some atrial diseases may be caused by a fundamental
395 disruption of atrial CM identity. More generally, we propose the notion that perturbations to cell
396 identity may serve as a basis for genetic susceptibility underlying some human diseases.
397

398 **STUDY LIMITATIONS**. Several limitations of this study should be considered. Although this
399 human cellular model mimics certain disease phenotypes, ASDs and AF manifest in a 3-
400 dimensional tissue and cannot be fully recapitulated in a 2-dimensional model system. Moreover,
401 certain *in vivo* cell types may be missing or represented poorly *in vitro*. Likewise, contributions
402 from the spatial organization of cells *in vitro* or heart tissue *in vivo* are not captured. Given that
403 there are several sub-categories of ASDs (e.g. primum ASD, secundum ASD, sinus venosus
404 ASD, or coronary sinus ASD) or AF (e.g. persistent AF, paroxysmal AF, or post-operative AF), it
405 remains to be determined how well this cellular disease model may reflect these conditions.
406 Further, by using scRNA-seq and snATAC-seq separately, this single cell approach uncovers

407 correlations between gene expression and chromatin accessibility, rather than directly linking
408 gene expression to chromatin accessibility in the same cell.
409
410 **METHODS**.
411 **iPSC culture and atrial cardiomyocyte differentiation**. Human iPSCs (WTC11, *TBX5*$^{in/+}$ and
412 *TBX5*$^{in/del}$) (Kathiriya et al., 2021) were maintained in mTESR Plus medium (Stemcell
413 Technologies, 100-0276). For directed differentiations, iPSCs were passaged on to GFR Matrigel-
414 coated 6-well plates until 70% confluency and then differentiated according to manufacturer's
415 instructions using the Stemdiff Atrial Cardiomyocyte Differentiation Kit (StemCell Technologies,
416 100-0215).
417
418 **Immunostaining**. Differentiated cells at day 20 from WTC11, *TBX5*$^{in/+}$ and *TBX5*$^{in/del}$ iPSCs were
419 dissociated using 0.25% trypsin and quenched with cardiomyocyte maintenance medium
420 containing 10% FBS. Cells were resuspended in cardiomyocyte maintenance medium with 10μM
421 ROCK inhibitor (StemCell Technologies, Y-27632), counted and plated onto growth factor-
422 reduced basement membrane matrix (GFR) Matrigel (Corning, 356231) coated-chambered slides
423 (Ibidi, 80381). Medium was replaced after 24 hours with fresh cardiomyocyte maintenance
424 medium. On the following day, cells were fixed in 4% formaldehyde for 15 minutes and washed
425 with PBS. Cells were then incubated in blocking buffer containing 5% goat serum and 0.1% Triton
426 X-100 in PBS for 1 hour at room temperature. Primary antibodies (alpha actinin, Sigma, A7811;
427 1:200 MLC2-V, Abcam, ab79935; ANP, GeneTex, GTX109255; 1:500 cTNT, Thermo, MS-295-
428 P) in blocking buffer were incubated with cells for 2 hours at room temperature. Following washes
429 in blocking buffer, cells were incubated in secondary antibodies at 1:200 dilution (goat anti mouse
430 Alexa Fluor 488, ThermoFisher, A11029, goat anti mouse Alexa Fluor 594, ThermoFisher,
431 A11005). Cells were then washed with blocking buffer and stained with DAPI at a 1:1000 dilution
432 for 2 minutes. Images were acquired using an Olympus FV3000RS and processed with ImageJ.
433 Evaluations of sarcomere disarray or cell size was performed as described previously (Kathiriya
434 et al., 2021) at day 20.
435
436 **Replating for multi-electrode array (MEA)**. iPSC-cardiomyocytes were harvested as described
437 above. An 8uL droplet of GFR Matrigel in KO DMEM was placed in the center of each well of a
438 BioCircuit MEA Plate (Axion Biosystems, M384-BIO-24) and incubated for 2 hrs at 37C. GFR was
439 gently removed and approximately 50,000 cells in 8-10ul droplets was placed in the center of
440 each well and incubated for 1 hr at 37C. After incubation, additional StemDiff maintenance media

441 with ROCKi was added to each well and incubated for 24 hrs at 37C. Subsequent media changes
442 were performed every other day with StemDiff maintenance media. MEA recordings were
443 acquired after at least 7 days of maintenance.
444
445 **MEA Electrophysiology**. Electrophysiological data was recorded on the Maestro Edge Micro
446 Electrode Array device (Axion Biosystems). Live recordings of iPSC-cardiomyocyte field
447 potentials and local extracellular action potentials (LEAPs) were acquired using the Cardiac
448 module in the AxIS Navigator Tool. Representative field potential and LEAP tracings from
449 recordings were acquired using the Axion Biosystems Cardiac Analysis Tool. Data collection and
450 analysis was performed using the MEA software (Axion Biosystems) according to manufacturer
451 instructions.
452
453 **Fluorescent *in-situ* hybridization**. iPSC-derived cardiomyocytes were harvested as described
454 above. Approximately 100,000 cells were then plated on to 3-well chambered slides with
455 removable silicone (Ibidi 80381). Cells were then fixed with 10% neutral buffered formalin for 30
456 minutes at room temperature, followed by washes with 1X PBS. Serial dehydration with 50%,
457 70% and 100% ethanol was performed, and slides were stored in 100% ethanol at -20C. On the
458 day of staining, cells were serially rehydrated and pretreated with hydrogen peroxide for 10
459 minutes and protease III for 10 minutes at a 1:5 dilution ratio. RNAscope Multiplex Fluorescent
460 Reagent Kit v2 (Advanced Cell Diagnostics, 323100) was used to detect *TNNT2* (518991),
461 *ANGPT1* (482901-C2), *DES* (403041-C2), *MEG3* (400821) and *NR2F1* (583751). Finally, silicone
462 chambers were removed from slides, and a coverslip was mounted using Prolong Gold anti-fade
463 mountant. Slides were imaged at 40X magnification on an Olympus FV3000RS confocal
464 microscope and analyzed using FIJI.
465
466 **Harvesting cells for single-cell RNA and ATAC sequencing**. Human iPSCs from WTC11,
467 $TBX5^{in/+}$ and $TBX5^{in/del}$ were differentiated using the Stemdiff Atrial Cardiomyocyte Differentiation
468 Kit (Stemcell Technologies 100-0215) or the Stemdiff Ventricular Cardiomyocyte Differentiation
469 Kit (Stemcell Technologies 05010). For atrial differentiations, cells were harvested from all three
470 genotypes at day 20 for scRNA- and snATAC-sequencing, and from WTC11 and $TBX5^{in/+}$ at day
471 45 for scRNA-sequencing, according to manufacturer instructions (10X Genomics). For
472 ventricular differentiations, cells were harvested from all three genotypes at day 23 for snATAC-
473 sequencing. Two replicates of 10,000 cells per genotype were collected for each timepoint, in two
474 experimental batches. Cells were dissociated using 0.25% trypsin, quenched with cardiomyocyte

475 maintenance medium containing 10% FBS and then counted. Cell suspensions were processed
476 for single-cell RNA sequencing using Chromium Next GEM Single Cell 3' GEM, Library & Gel
477 Bead Kit v3.1 (10X Genomics). For single nuclei ATAC-sequencing, nuclei were harvested and
478 processed according to manufacturer's instructions using the Chromium Next GEM Single Cell
479 ATAC Library & Gel Bead Kit v1.1 (10X Genomics). Libraries were sequenced on an Illumina
480 Novaseq6000 S4 or Novaseq X.
481
482 **Analysis of single-cell RNA sequencing data**. Fastq files were processed using Cellranger
483 count (v6.1.1). Counts from samples from a single timepoint were aggregated using Cellranger
484 aggr without read-depth normalization. Seurat (v4.4) (Hao et al., 2021) was used to analyze the
485 data. Cells with low UMI count plus a high percentage of mitochondrial reads were considered
486 dying and removed. Potential doublets with aberrantly high gene counts were also removed.
487 Normalization was performed using SCTransform and batch effects were corrected using the
488 SeuratWrapper function RunHarmony. After annotating major cell types, *TNNT2*$^{+}$ clusters were
489 subset and further analyzed. Differentially expressed genes with an adjusted $p<0.05$ from
490 Wilcoxon rank-sum test were reported.
491 In Figure 1, single cell RNA sequencing data from WT atrial differentiation was merged
492 and analyzed with previously generated data from WT ventricular differentiation (Kathiriya et al.,
493 2021). Differentially expressed genes were obtained by comparing atrial CM clusters with
494 ventricular CM clusters. In Figure 3, WT cells from clusters highly enriched for *MYH6* were
495 compared to *TBX5*$^{in/+}$ or *TBX5*$^{in/del}$ cells from other clusters with *MYH6*, similar to the Monocle
496 partitions in Figure 3D.
497 Volcano plots were generated using the EnhancedVolcano package. Differential genes
498 were intersected with curated lists containing CHD-associated genes, atrial fibrillation-risk genes
499 and genes associated with atrial septal defects. CHD-associated gene list includes our previously
500 curated list from Kathiriya et al., 2021, and genes from the CHDgene database
501 (http://chdgene.victorchang.edu.au/) (Yang et al., 2022). Atrial fibrillation-risk genes were
502 gathered from the Harmonizome database (https://maayanlab.cloud/Harmonizome/), and
503 (Ouwerkerk et al., 2019; Ouwerkerk et al., 2020; Roselli et al., 2018) (Supp. Data 5). The MiloR
504 package (v2.0.0) (Dann et al., 2022) was used for differential cell type abundance testing. The
505 precomputed KNN graph from Seurat was imported using the buildFromAdjacency function. The
506 number of nearest neighbors k was set to 40. Differential abundance results were visualized by
507 setting alpha = 0.05. Monocle 3 (v1.3.7) (Cao et al., 2019) was used for pseudotime analysis.
508 Cells in the atrial precursor-like clusters were chosen as root cells for each Monocle 3 partition

using the “order_cells” function. Pseudotime was visualized on the UMAP using the “plot_cells” function.

Cell abundance testing. A Generalized Linear Mixed Effects Model (GLMM) was implemented in the lme4 (version 1.1-37) R package (Bates et al., 2015) and was used to estimate the associations between cell type-annotations and *Tbx5* genotype (WT, Het or Hom). These models were run separately for each cluster of cells identified within the full data or within subtypes of CMs. The family argument was set to the binomial probability distribution for the GLMM model fit. Cluster membership of cells by sample was modeled as a response variable by a two-dimensional vector representing the number of cells from the given sample belonging to and not belonging to the cluster under consideration. The corresponding sample ID from which the cell was derived was the random effect variable, and the genotype was included as the fixed variable. The resulting P values for the significance estimated log odds ratios were adjusted for multiple testing using the Benjamini–Hochberg method (Benjamini and Hochberg, 1995).

Analysis of single-cell ATAC sequencing data. Fastq files were processed using Cellranger ATAC count (v2.0). Data was analyzed by following the tutorial for ArchR (v1.0.2) (Granja et al., 2021). Pseudobulk replicates for each genotype in each cluster were generated with a minimum of 500 and maximum of 1000 cells for each replicate. Peaks were called with MACS2 by setting reproducibility to 2. Volcano plots show differential peaks with FDR < 0.1 and log2FC >0.25. Motif annotations were added from CIS-BP repository using the addMotifAnnotations function and motif enrichment in differential peaks was performed using the peakAnnoEnrichment function with FDR <0.1 and log2FC >0.25. Overlapping ATAC (this manuscript) and TBX5 ChIP peaks (Grant et al., 2025) were attained using findOverlaps from the Genomic ranges package. Browser tracks were generated using IGV Desktop application. In Figure 1, differentially accessible regions were reported between atrial CM clusters and ventricular CM clusters. In Figure 5, differentially accessible regions were reported between WT cells in WT-enriched (C2+C3) clusters and *TBX5*$^{in/+}$ cells in *TBX5*$^{in/+}$-enriched (C6) clusters or *TBX5*$^{in/del}$ cells in *TBX5*$^{in/del}$ -enriched (C5) clusters.

Gene regulatory network analysis. Gene regulatory network analysis was performed using the CellOracle (v0.18.0) package (Kamimoto et al., 2023). Default parameters were used according to the documentation, unless specified otherwise. For wildtype atrial CM- and ventricular CM-specific GRNs, base GRNs were constructed using scATAC-seq data at day 20 from WTC11

atrial CM and ventricular CM subsets, respectively (Supp. Data 3). Cell type-specific GRNs were then constructed by setting alpha = 1000. For *TBX5* genotype-specific GRNs, base GRNs were constructed using scATAC-seq data at day 20 from WTC11 cells (Supp. Data 7). The apparent upregulation of *TBX5* mRNA presumably from non-mutated exons (Kathiriya 2021) in *TBX5* heterozygous mutants was manually corrected by halving the raw counts in $Tbx5^{in/+}$ and setting the raw counts to zero in $Tbx5^{in/del}$ cells, consistent with Western blot data (Fig S1A, B). Cell type-specific GRNs were then constructed by setting alpha = 1000.

Inferred GRNs were filtered to include only the 12,000 edges with largest absolute coefficient values. Centrality calculations for the 12,000 edge networks were calculated using CellOracle's links.get_network_score() function. PyVis (Perrone et al., 2020) was used to visualize subnetworks. The large nodes in these networks were manually selected TFs and small nodes are the direct targets in the 12,000-edge networks. The edge color was selected to indicate whether a TF activated (grey) or inhibited (red) a target, and edge thickness was scaled based on absolute coefficient magnitude. For networks in (Fig 1T, U), we chose canonical atrial or ventricular TFs, along with some novel TFs - *TBX5, NR2F2*, *MEF2C*, *NKX2-5*, *MEIS2*, *GATA4*, *HAND1*, *IRX4*, *HEY2*, *PLAGL1*, *NR2F1*, *HES4*, *E2F1*, and *HEY1*. For networks in Fig 6A-C, the manually selected TFs included *TBX5*, *NR2F2*, *MEF2C, NKX2-5, MEIS2, GATA4, HAND1, IRX4, HEY2, PLAGL1, NR2F1, HES4, E2F1, HEY1, TCF21, TEAD1*, and *TCF12.* For Fig 6D-F, we identified TFs that had source or target connections to TBX5 (Supp. Data 7) and prioritized ones that displayed dose-dependent change in centrality by *TBX5* genotype and are CHD- or AF- risk genes. These networks exclude the TFs and only show direct connections between prioritized genes. Wheel diagrams that display direct interactions between TFs and their targets were developed using Python's NetworkX package (Hagberg et al., 2008), with a circular layout and edge widths scaled by coefficient values.

ACKNOWLEDGEMENTS. We thank members of the Bruneau and Kathiriya labs for discussion and comments, and of the Gladstone Stem Cell Core, Histology and Microscopy, and Flow Cytometry Core and the UCSF Center for Advanced Technologies for their expert assistance. We thank Reuben Thomas of the Gladstone Bioinformatics Core for valuable feedback on statistical analyses. The Gladstone Flow Cytometry Core is funded by NIH S10 RR028962, the James B. Pendleton Charitable Trust and DARPA. Sequencing was performed at the UCSF CAT, supported by UCSF PBBR, RRP IMIA, and NIH 1S10OD028511-01 grants.

576 **COMPETING INTERESTS.** B.G.B. is a co-founder and shareholder of Tenaya Therapeutics, and
577 none of the work presented here is related to those interests.
578
579 **FUNDING.** This work was supported by grants from the National Institutes of Health (NHLBI U01
580 HL157989 to B.G.B and I.S.K; NHLBI R01 HL155906 to B.G.B. and I.S.K., T32HL007284 to
581 A.P.C.; R01HL160665 and R01HL162925 to J.J.S.), The Roddenberry Foundation (B.G.B.), the
582 Younger Family Fund (B.G.B.), Additional Ventures Innovation Award (B.G.B), California Institute
583 for Regenerative Medicine (Z.L.G.), Additional Ventures Catalyst to Independence Award
584 (Z.L.G.), American Heart Association (S.K.H.), Startup and seed funding from Indiana University
585 (S.K.H.), Hellman Family Fund (I.S.K.), UCSF Pediatric Heart Center Catalyst Award (I.S.K),
586 Saving tiny Hearts Society (I.S.K.) and UCSF Anesthesia Research Support (I.S.K.).
587
588 **DATA AND RESOURCE AVAILABILITY.** Cell lines are available under a material transfer
589 agreement. All relevant data is available on NCBI GEO (Accession GSE285168 and GSE285169)
590 and details of the code are available at GitHub (apclarkva/kathiriya-rao-2025).
591
592 **Fig. 1. Features of gene expression and chromatin accessibility in human iPSC-derived**
593 **atrial cardiomyocytes (CMs) predict TBX5-sensitive atrial CM identity**. Directed
594 differentiations of human induced pluripotent stem cells (iPSCs) to ventricular or atrial cells were
595 assessed by immunostaining of (A-G) ANP or (H-N) MLC2V (****$p<0.0001$ by Fisher's exact test).
596 (O,P) Normalized local extracellular action potential (LEAP) by cell type. (Q) Violin plot of
597 ventricular- or atrial-enriched CM genes. (R) Overlapping chromatin accessible regions. Bar plot
598 shows number of common accessible regions by less than 90% overlap or greater than or equal
599 to 90% overlap. (S) Motifs enriched in differentially accessible regions (DARs) (FDR<0.1). Gene
600 regulatory networks of (T) ventricular or (U) atrial CMs. Wheel diagrams for *TBX5* show a shift in
601 significant direct connections between (V) ventricular and (W) atrial CMs. Based on input of UMAP
602 of atrial CM cell types in (X) wildtype, *in silico* prediction by CellOracle infers the states of
603 individual cells from atrial cardiomyotyces (CMs) to CMs expressing extracellular matrix genes
604 (CMEs) by complete *TBX5* loss (*TBX5*=0)(Y).
605
606 **Fig. S1. Gene expression, chromatin accessibility and GRN analyses in ventricular or atrial**
607 **CMs.** UMAPs of scRNA-seq annotated by (A) cell types or by (B) differentiation to ventricular or
608 atrial cells. (C) UMAP of snATAC-seq by inferred cell type from gene score, or by (D)
609 differentiation. (E) UMAP of gene scores from snATAC-seq for *MYL2* (ventricular CM-enriched)

610 and *MYH6* (atrial CM-enriched). UMAP of snRNA-seq subset of *TNNT2*$^{+}$-gene score^{+} cells
611 inferred as CMs from ventricular or atrial differentiation (F) or by Louvain cell clustering (G). (H)
612 Bar plot of snATAC-seq peak distribution in the genome by cell cluster. (I) Volcano plot of
613 differential accessible regions enriched in ventricular or atrial CMs (FDR<0.1). Centrality scores
614 of TFs by (J) betweenness or (K) degree out. Wheel diagrams of *HEY2* (L, M) or *HEY1* (N, O)
615 direct connections in ventricular or atrial CMs.
616
617 **Fig. S2. Analysis of a human cellular model of atrial disease.** (A) Western blot and (B)
618 quantification of TBX5 by *TBX5* genotype (*p<0.05 by Welch's T-test). (C) Bar plot shows cell
619 types at day 20 by *TBX5* genotypes.
620
621 **Fig. 2. Modeling genetic susceptibility to reduced TBX5 in human atrial cells.** (A)
622 Differentiation efficiency by flow cytometry of cTNT (**p<0.01, ***p<0.001 by Student's T-test).
623 (B-E) cTNT immunostaining shows sarcomeric disarray in *TBX5* mutant atrial CMs (*p<0.05,
624 ****p<0.0001 by Fisher's exact test). (F) Average cell area is significantly increased in *TBX5*
625 mutant atrial CMs (*p<0.05, ****p<0.0001 by Student's T-test). (G, H) Typical action potential
626 traces by MEA. (I-J) Field potential and normalized local extracellular action potential durations
627 at 90% (APD_{90}) are increased in *TBX5* heterozygous mutant atrial CMs (****p<0.0001 by Welch's
628 T-test). (K) UMAP displays scRNA-seq data at day 20 by (K) *TBX5* genotype or (L) cell type
629 labels. (M) Dot plot of genes used to define cell types. (N) Distribution of cell types by *TBX5*
630 genotypes shows reduced CMs and increased fibroblasts and epithelial-like cells in *TBX5*$^{in/del}$
631 (***adj. p<0.001 by linear regression). *TBX5*$^{in/+}$ remains largely similar to WT. (O,P) Milo analysis
632 showed a statistically significant difference in the abundance of CMs, fibroblasts, epithelial and
633 neural-like cells for *TBX5*$^{in/del}$ (FDR<0.05).
634
635 **Fig. 3. Atrial CM identity by gene expression is vulnerable to reduced TBX5 dosage.** UMAP
636 of *TNNT2*+ cells colored by (A) genotype, (B) cell type markers or (C) cell type labels. (D)
637 Monocole 3 analysis shows the predominant pseuodtime paths (i.e., in pseudocolor, represented
638 by the arrows) in two partitions affected in *TBX5*$^{in/del}$. Specifically, in partition 1, fewer WT cells
639 reach the end of the path to CME-3, compared to *TBX5*$^{in/del}$. In partition 2, fewer *TBX5*$^{in/del}$ cells
640 reach the end of the pseudotime path to *NPPA*$^{+}$ CMs. (E) Cell numbers of many atrial CM cell
641 types are significantly reduced in *TBX5* mutants. (*adj. p<0.05 **adj. p<0.01, ***adj. p<0.001 by
642 linear regression). (E, F) Volcano plots show differentially expressed genes in *TBX5* mutants (adj.
643 p-value by Wilcoxan rank sum). (G) Categories of down- and up-regulated genes in *TBX5*$^{in/+}$ or

644 *TBX5*$^{in/del}$ (adj. p<0.05 by Wilcoxan rank sum). (H-J) AF- and CHD-risk genes are enriched among
645 differentially expressed TBX5-sensitive genes (p-value by hypergeometric test). Dot plots of
646 differentially-expressed CHD, ASD (in green) and AF genes in (K) *TBX5*$^{in/+}$ or (L) in both *TBX5*$^{in/+}$
647 and *TBX5*$^{in/del}$ (adj. p<0.05 by Wilcoxan rank sum).
648
649 **Fig. S3. Analysis of CMs in a human cellular model of atrial disease.** (A) Bar plot shows CM
650 sub-types at day 20 by *TBX5* genotypes.
651
652 **Fig. 4. Fluorescent *in situ* hybridization of TBX5-dependent genes.** Gene expression in WT
653 or *TBX5* mutants of *TNNT2* and *NR2F1* (A-C), *DES* (D-F), *MEG3* (G-J), and *ANGPT1* (K-N)
654 (***p<0.001 by Fisher's exact test).
655
656 **Fig. S4. *TBX5* heterozygous mutants at day 45 by scRNA-seq**. UMAP by (A) genotype or (B)
657 cell type label at day 45. (C) Feature plots of marker genes for cell type labels. (D) Bar plot shows
658 distribution of cell types in WT or *TBX5*$^{in/+}$, including a reduction in CMs in *TBX5* mutants (*adj.
659 p<0.05, ***adj. p<0.001 by linear regression). UMAP of CM sub-types by (E) genotype or (F) CM
660 sub-type labels. (G) Feature plot of marker genes for CM sub-type labels. (H) Bar plot shows
661 distribution of CM sub-types in WT or *TBX5*$^{in/+}$, including alterations to several CM sub-types
662 (**adj. p<0.01, ***adj. p<0.001 by linear regression). (I) Volcano plot shows diferentially expressed
663 genes (adj. p-value by Wilcoxan rank sum). Dot plots of differentially-expressed CHD, ASD (in
664 green) and AF genes in (J) *TBX5*$^{in/+}$ (adj. p<0.05 by Wilcoxan rank sum).
665
666 **Fig. S5. Comparison of *TBX5* heterozygous mutants at day 20 and day 45**. Venn diagrams
667 of altered genes for (A) CHD-risk or (B) AF-risk (p-value by hypergeometric test). UMAP of CM
668 sub-types in merged data of day 20 and day 45 by (C) *TBX5* genotype and (D) CM sub-type
669 labels. (E) Dot plots of differentially-expressed CHD, ASD (in green) and AF genes in *TBX5*$^{in/+}$ in
670 merged data of day 20 and day 45 (adj. p-value<0.05 by Wilcoxan rank sum).
671
672 **Fig. 5. TBX5 dosage-sensitive chromatin accessibility in human atrial cells**. UMAP of all
673 atrial cells colored by (A) *TBX5* genotype or (B) cluster. UMAP of *TNNT2*$^{+}$-gene score cells
674 colored by (C) *TBX5* genotype or (D) cluster. (E-F) Motifs enriched in differentially accessible
675 regions (DARs) in (E) *TBX5*$^{in/del}$ or (F) *TBX5*$^{in/+}$ (FDR<0.1). DARs with (G) predicted TBX/MEIS
676 motifs or (G') with TBX5 occupancy. Browser track showing scATAC peaks near (H) NPPA-NPPB

677 or (I) NR2F1. Gray shading indicates DARs. TBX5 occupancy in WT cells by TBX5 ChIP-seq
678 (Grant et al. 2024).
679
680 **Fig. S6. Analysis of chromatin accessibility in *TBX5* mutant atrial cells.** (A) Feature plots of
681 gene scores identify putative cell types from chromatin accessibility. (B) Feature plots of gene
682 scores identify putative CM sub-types from chromatin accessibility. (C) Genomic distribution of
683 peaks by cluster. Differentially accessible peaks in (D) $TBX5^{in/+}$ or (E) $TBX5^{in/del}$. (F-I) Overlap of
684 genes near DARs and differential gene expression in *TBX5* mutants. (J, K) Overlap of DARs in
685 $TBX5^{in/+}$ and $TBX5^{in/del}$.
686
687 **Fig. 6. Proper TBX5 dosage controls disease-linked atrial CM gene regulatory networks**
688 **(GRNs).** (A-C) GRNs of atrial CMs with selected TFs by *TBX5* genotype. Grey lines indicate
689 positive correlations. Red lines depict negative correlations. Genes that are edges are unlabeled
690 for simplicity of diagram. (D-F) Priority networks of atrial CMs shows TF sources to TBX5 or CHD-
691 , ASD- (in green) or AF-risk genes in *TBX5* mutants. (G) Betweenness or (H) degree out centrality
692 of selected TFs in GRNs. Wheel diagrams of (I) *TBX5* or (J) *NR2F1*. Strength of black arrows
693 depicts strength of positive correlation, while strength of red arrows depicts strength of negative
694 correlations.
695
696 **Fig. S7. Network analysis of *TBX5* mutants in human atrial CMs.** Venn diagrams show overlap
697 of (A) nodes or (B) edges in the same direction in *TBX5* mutants. Wheel diagrams of (E) ASD-
698 and AF-risk *NKX2-5*, (F) ASD-risk *NR2F2*, (G) fibroblast-associated TCF21, and (H) fibroblast-
699 associated TCF12. Strength of black arrows depicts strength of positive correlation, while strength
700 of red arrows depicts strength of negative correlations.
701
702 **Supplementary Data 1**. Table of differentially expressed genes between an $MYH6^{+}$-enriched
703 cluster of atrial CMs and an $MYL2^{+}$-enriched cluster of ventricular CMs.
704
705 **Supplementary Data 2**. Table of differentially accessible regions between *MYH6*-gene $score^{+}$
706 atrial CM and *MYL2*-gene $score^{+}$ ventricular CM clusters.
707
708 **Supplementary Data 3**. Table of sources and targets in networks for atrial CM or ventricular CM
709 clusters.
710

711 **Supplementary Data 4**. Table of differentially expressed genes among *TNNT2*$^{+}$ clusters by TBX5
712 genotype.
713
714 **Supplementary Data 5**. Lists of disease-risk genes for CHDs, ASDs, AF, and ASDs and AF.
715
716 **Supplementary Data 6**. Table of differentially accessible regions of *TNNT2*-gene score^{+} CM
717 clusters by *TBX5* genotype.
718
719 **Supplementary Data 7**. Table of sources and targets in networks for CM clusters from atrial CM
720 differentiation by *TBX5* genotype.
721
722
723 **BIBLIOGRAPHY**
724

725 **Bartholin, L., Powers, S. E., Melhuish, T. A., Lasse, S., Weinstein, M. and Wotton, D.**
726 (2006). TGIF Inhibits Retinoid Signaling. *Mol. Cell. Biol.* **26**, 990–1001.

727 **Basson, C. T., Cowley, G. S., Solomon, S. D., Weissman, B., Poznanski, A. K., Traill, T. A.,**
728 **Seidman, J. G. and Seidman, C. E.** (1994). The clinical and genetic spectrum of the Holt-
729 Oram syndrome (heart-hand syndrome). *N Engl J Med* **330**, 885–891.

730 **Basson, C. T., Bachinsky, D. R., Lin, R. C., Levi, T., Elkins, J. A., Soults, J., Grayzel, D.,**
731 **Kroumpouzou, E., Traill, T. A., Leblanc-Straceski, J., et al.** (1997). Mutations in human
732 TBX5 [corrected] cause limb and cardiac malformation in Holt-Oram syndrome. *Nat Genet*
733 **15**, 30–35.

734 **Bates, D., Mächler, M., Bolker, B. and Walker, S.** (2015). Fitting Linear Mixed-Effects Models
735 Using lme4. *J. Stat. Softw.* **67**,.

736 **Benjamini, Y. and Hochberg, Y.** (1995). Controlling the False Discovery Rate - a Practical and
737 Powerful Approach to Multiple Testing. *Journal of the Royal Statistical Society Series B-*
738 *Statistical Methodology* **57**, 289–300.

739 **Benson, D. W., Sharkey, A., Fatkin, D., Lang, P., Basson, C. T., McDonough, B., Strauss,**
740 **A. W., Seidman, J. G. and Seidman, C. E.** (1998). Reduced penetrance, variable
741 expressivity, and genetic heterogeneity of familial atrial septal defects. *Circulation* **97**, 2043–
742 2048.

743 **Benson, D. W., Wang, D. W., Dyment, M., Knilans, T. K., Fish, F. A., Strieper, M. J.,**
744 **Rhodes, T. H. and George, A. L.** (2003). Congenital sick sinus syndrome caused by
745 recessive mutations in the cardiac sodium channel gene (SCN5A). *J. Clin. Investig.* **112**,
746 1019–1028.

Bersell, K. R., Yang, T., Mosley, J. D., Glazer, A. M., Hale, A. T., Kryshtal, D. O., Kim, K., Steimle, J. D., Brown, J. D., Salem, J.-E., et al. (2023). Transcriptional Dysregulation Underlies Both Monogenic Arrhythmia Syndrome and Common Modifiers of Cardiac Repolarization. *Circulation* **147**, 824–840.

Bever, Y. van, Dijkstra, P. F. and Hennekam, R. C. M. (1996). Autosomal dominant familial radial luxation, carpal fusion and scapular dysplasia with variable heart defects. *Am. J. Méd. Genet.* **65**, 213–217.

Boniel, S., Szymańska, K., Śmigiel, R. and Szczałuba, K. (2021). Kabuki Syndrome—Clinical Review with Molecular Aspects. *Genes-basel* **12**, 468.

Briganti, F., Sun, H., Wei, W., Wu, J., Zhu, C., Liss, M., Karakikes, I., Rego, S., Cipriano, A., Snyder, M., et al. (2020). iPSC Modeling of RBM20-Deficient DCM Identifies Upregulation of RBM20 as a Therapeutic Strategy. *Cell Rep.* **32**, 108117.

Bruneau, B. G., Nemer, G., Schmitt, J. P., Charron, F., Robitaille, L., Caron, S., Conner, D. A., Gessler, M., Nemer, M., Seidman, C. E., et al. (2001). A Murine Model of Holt-Oram Syndrome Defines Roles of the T-Box Transcription Factor Tbx5 in Cardiogenesis and Disease. *Cell* **106**, 709–721.

Burstein, B., Libby, E., Calderone, A. and Nattel, S. (2008). Differential Behaviors of Atrial Versus Ventricular Fibroblasts. *Circulation* **117**, 1630–1641.

Bushdid, P. B., Osinska, H., Waclaw, R. R., Molkentin, J. D. and Yutzey, K. E. (2003). NFATc3 and NFATc4 Are Required for Cardiac Development and Mitochondrial Function. *Circ. Res.* **92**, 1305–1313.

Cao, J., Spielmann, M., Qiu, X., Huang, X., Ibrahim, D. M., Hill, A. J., Zhang, F., Mundlos, S., Christiansen, L., Steemers, F. J., et al. (2019). The single-cell transcriptional landscape of mammalian organogenesis. *Nature* **34**, 65–31.

Chen, Y.-H., Xu, S.-J., Bendahhou, S., Wang, X.-L., Wang, Y., Xu, W.-Y., Jin, H.-W., Sun, H., Su, X.-Y., Zhuang, Q.-N., et al. (2003). KCNQ1 Gain-of-Function Mutation in Familial Atrial Fibrillation. *Science* **299**, 251–254.

Ching, Y.-H., Ghosh, T. K., Cross, S. J., Packham, E. A., Honeyman, L., Loughna, S., Robinson, T. E., Dearlove, A. M., Ribas, G., Bonser, A. J., et al. (2005). Mutation in myosin heavy chain 6 causes atrial septal defect. *Nat Genet* **37**, 423–428.

Choi, S. H., Weng, L.-C., Roselli, C., Lin, H., Haggerty, C. M., Shoemaker, M. B., Barnard, J., Arking, D. E., Chasman, D. I., Albert, C. M., et al. (2018). Association Between Titin Loss-of-Function Variants and Early-Onset Atrial Fibrillation. *Jama* **320**, 2354.

Cyganek, L., Tiburcy, M., Sekeres, K., Gerstenberg, K., Bohnenberger, H., Lenz, C., Henze, S., Stauske, M., Salinas, G., Zimmermann, W.-H., et al. (2018). Deep phenotyping of human induced pluripotent stem cell–derived atrial and ventricular cardiomyocytes. *JCI Insight* **3**, 1–18.

Dai, W., Laforest, B., Tyan, L., Shen, K. M., Nadadur, R. D., Alvarado, F. J., Mazurek, S. R., Lazarevic, S., Gadek, M., Wang, Y., et al. (2019). A calcium transport mechanism for atrial fibrillation in Tbx5-mutant mice. *eLife* **8**, 40.

Dann, E., Henderson, N. C., Teichmann, S. A., Morgan, M. D. and Marioni, J. C. (2022). Differential abundance testing on single-cell data using k-nearest neighbor graphs. *Nat. Biotechnol.* **40**, 245–253.

DeLaughter, D. M., Bick, A. G., Wakimoto, H., McKean, D., Gorham, J. M., Kathiriya, I. S., Hinson, J. T., Homsy, J., Gray, J., Pu, W., et al. (2016). Single-Cell Resolution of Temporal Gene Expression during Heart Development. *Dev Cell* **39**, 1–25.

Desjardins, C. and Naya, F. (2016). The Function of the MEF2 Family of Transcription Factors in Cardiac Development, Cardiogenomics, and Direct Reprogramming. *JCDD* **3**, 26–19.

Devalla, H. D., Gélinas, R., Aburawi, E. H., Beqqali, A., Goyette, P., Freund, C., Chaix, M. A., Tadros, R., Jiang, H., Béchec, A. L., et al. (2016). TECRL, a new life-threatening inherited arrhythmia gene associated with overlapping clinical features of both LQTS and CPVT. *EMBO Mol Med* **8**, 1390–1408.

Dobrev, D., Aguilar, M., Heijman, J., Guichard, J.-B. and Nattel, S. (2019). Postoperative atrial fibrillation: mechanisms, manifestations and management. *Nat Rev Cardiol* **16**, 1–20.

Friedman, C. E., Fayer, S., Pendyala, S., Chien, W.-M., Loiben, A., Tran, L., Chao, L. S., McKinstry, A., Ahmed, D., Farris, S. D., et al. (2024). Multiplexed Functional Assessments of MYH7 Variants in Human Cardiomyocytes. *Circ.: Genom. Precis. Med.* **17**, e004377.

Garg, V., Kathiriya, I. S., Barnes, R., Schluterman, M. K., King, I. N., Butler, C. A., Rothrock, C. R., Eapen, R. S., Hirayama-Yamada, K., Joo, K., et al. (2003). GATA4 mutations cause human congenital heart defects and reveal an interaction with TBX5. *Nature* **424**, 443–447.

Garg, V., Muth, A. N., Ransom, J. F., Schluterman, M. K., Barnes, R., King, I. N., Grossfeld, P. D. and Srivastava, D. (2005). Mutations in NOTCH1 cause aortic valve disease. **437**, 270–274.

Gise, A. von, Lin, Z., Schlegelmilch, K., Honor, L. B., Pan, G. M., Buck, J. N., Ma, Q., Ishiwata, T., Zhou, B., Camargo, F. D., et al. (2012). YAP1, the nuclear target of Hippo signaling, stimulates heart growth through cardiomyocyte proliferation but not hypertrophy. *Proc. Natl. Acad. Sci.* **109**, 2394–2399.

Goldfracht, I., Protze, S., Shiti, A., Setter, N., Gruber, A., Shaheen, N., Nartiss, Y., Keller, G. and Gepstein, L. (2019). Generating ring-shaped engineered heart tissues from ventricular and atrial human pluripotent stem cell-derived cardiomyocytes. *Nat Commun* 1–15.

Granja, J. M., Corces, M. R., Pierce, S. E., Bagdatli, S. T., Choudhry, H., Chang, H. Y. and Greenleaf, W. J. (2020). ArchR: An integrative and scalable software package for single-cell chromatin accessibility analysis. **37**, 916–86.

822 **Granja, J. M., Corces, M. R., Pierce, S. E., Bagdatli, S. T., Choudhry, H., Chang, H. Y. and**
823 **Greenleaf, W. J.** (2021). ArchR is a scalable software package for integrative single-cell
824 chromatin accessibility analysis. *Nat Genet* **53**, 403–411.

825 **Grant, Z. L., Kuang, S., Zhang, S., Horrillo, A. J., Rao, K. S., Kameswaran, V., Joubran, C.,**
826 **Lau, P. K., Dong, K., Yang, B., et al.** (2025). Dose-dependent sensitivity of human 3D
827 chromatin to a heart disease-linked transcription factor. *bioRxiv* 2025.01.09.632202.

828 **Gudbjartsson, D. F., Holm, H., Sulem, P., Masson, G., Oddsson, A., Magnusson, O. Th.,**
829 **Saemundsdottir, J., Helgadottir, H. Th., Helgason, H., Johannsdottir, H., et al.** (2016). A
830 frameshift deletion in the sarcomere gene MYL4 causes early-onset familial atrial fibrillation.
831 *Eur Heart J* **38**, 27–34.

832 **Guo, D.-F., Li, R.-G., Yuan, F., Shi, H.-Y., Hou, X.-M., Qu, X.-K., Xu, Y.-J., ZHANG, M., LIU,**
833 **X., JIANG, J.-Q., et al.** (2016). TBX5 loss-of-function mutation contributes to atrial fibrillation
834 and atypical Holt-Oram syndrome. *Mol Med Rep* **13**, 4349–4356.

835 **Hagberg, A. A., Schult, D. A. and Swart, P. J.** (2008). Exploring Network Structure, Dynamics,
836 and Function using NetworkX. *Proc. 7th Python Sci. Conf.* 11–15.

837 **Hao, Y., Hao, S., Andersen-Nissen, E., Mauck, W. M., Zheng, S., Butler, A., Lee, M. J., Wilk,**
838 **A. J., Darby, C., Zager, M., et al.** (2021). Integrated analysis of multimodal single-cell data.
839 *Cell* **184**, 3573-3587.e29.

840 **Hinson, J. T., Chopra, A., Nafissi, N., Polacheck, W. J., Benson, C. C., Swist, S., Gorham,**
841 **J., Yang, L., Schafer, S., Sheng, C. C., et al.** (2015). HEART DISEASE. Titin mutations in
842 iPS cells define sarcomere insufficiency as a cause of dilated cardiomyopathy. *Science* **349**,
843 982–986.

844 **Hnatiuk, A. P., Briganti, F., Staudt, D. W. and Mercola, M.** (2021). Human iPSC modeling of
845 heart disease for drug development. *Cell Chem. Biol.* **28**, 271–282.

846 **Hodgson-Zingman, D. M., Karst, M. L., Zingman, L. V., Heublein, D. M., Darbar, D., Herron,**
847 **K. J., Ballew, J. D., Andrade, M. de, Burnett, J. C. and Olson, T. M.** (2008). Atrial
848 Natriuretic Peptide Frameshift Mutation in Familial Atrial Fibrillation. *New Engl J Medicine*
849 **359**, 158–165.

850 **Hoffman, J. I. E. and Kaplan, S.** (2002). The incidence of congenital heart disease. *J Am Coll*
851 *Cardiol* **39**, 1890–1900.

852 **Hong, K., Bjerregaard, P., Gussak, I. and Brugada, R.** (2005). Short QT Syndrome and Atrial
853 Fibrillation Caused by Mutation in KCNH2. *J Cardiovasc Electr* **16**, 394–396.

854 **Horsthuis, T., Houweling, A. C., Habets, P. E. M. H., Lange, F. J. D., Azzouzi, H. el, Clout,**
855 **D. E. W., Moorman, A. F. M. and Christoffels, V. M.** (2008). Distinct Regulation of
856 Developmental and Heart Disease-Induced Atrial Natriuretic Factor Expression by Two
857 Separate Distal Sequences. *Circ Res* **102**, 849–859.

858 **Kamimoto, K., Stringa, B., Hoffmann, C. M., Jindal, K., Solnica-Krezel, L. and Morris, S. A.**
859 (2023). Dissecting cell identity via network inference and in silico gene perturbation. *Nature*
860 **614**, 742–751.

861 **Karakikes, I., Termglinchan, V., Cepeda, D. A., Lee, J., Diecke, S., Hendel, A., Itzhaki, I.,**
862 **Ameen, M., Shrestha, R., Wu, H., et al.** (2017). A Comprehensive TALEN-Based Knockout
863 Library for Generating Human-Induced Pluripotent Stem Cell-Based Models for
864 Cardiovascular Diseases. *Circ Res* **120**, 1561–1571.

865 **Kathiriya, I. S., Rao, K. S., Iacono, G., Devine, W. P., Blair, A. P., Hota, S. K., Lai, M. H.,**
866 **Garay, B. I., Thomas, R., Gong, H. Z., et al.** (2021). Modeling Human TBX5
867 Haploinsufficiency Predicts Regulatory Networks for Congenital Heart Disease. *Dev Cell* **56**,
868 292-309.e9.

869 **Kim, K. H., Nakaoka, Y., Augustin, H. G. and Koh, G. Y.** (2018). Myocardial Angiopoietin-1
870 Controls Atrial Chamber Morphogenesis by Spatiotemporal Degradation of Cardiac Jelly.
871 *Cell Rep.* **23**, 2455–2466.

872 **Kirk, E. P., Sunde, M., Costa, M. W., Rankin, S. A., Wolstein, O., Castro, M. L., Butler, T. L.,**
873 **Hyun, C., Guo, G., Otway, R., et al.** (2007). Mutations in cardiac T-box factor gene TBX20
874 are associated with diverse cardiac pathologies, including defects of septation and
875 valvulogenesis and cardiomyopathy. *Am J Hum Genet* **81**, 280–291.

876 **Knollmann, B. C.** (2013). Induced Pluripotent Stem Cell–Derived Cardiomyocytes. *Circ. Res.*
877 **112**, 969–976.

878 **Kornej, J., Börschel, C. S., Benjamin, E. J. and Schnabel, R. B.** (2020). Epidemiology of
879 Atrial Fibrillation in the 21st Century. *Circ. Res.* **127**, 4–20.

880 **Lan, F., Lee, A. S., Liang, P., Sanchez-Freire, V., Nguyen, P. K., Wang, L., Han, L., Yen, M.,**
881 **Wang, Y., Sun, N., et al.** (2013). Abnormal Calcium Handling Properties Underlie Familial
882 Hypertrophic Cardiomyopathy Pathology in Patient-Specific Induced Pluripotent Stem Cells.
883 *Cell Stem Cell* **12**, 101–113.

884 **Lee, J. H., Protze, S. I., Laksman, Z., Backx, P. H. and Keller, G. M.** (2017). Human
885 Pluripotent Stem Cell-Derived Atrial and Ventricular Cardiomyocytes Develop from Distinct
886 Mesoderm Populations. *Cell Stem Cell* **21**, 179-194.e4.

887 **Lee, S.-P., Ashley, E. A., Homburger, J., Caleshu, C., Green, E. M., Jacoby, D., Colan, S.**
888 **D., Arteaga-Fernández, E., Day, S. M., Girolami, F., et al.** (2018). Incident Atrial Fibrillation
889 Is Associated With MYH7 Sarcomeric Gene Variation in Hypertrophic Cardiomyopathy.
890 *Circulation Hear Fail* **11**, e005191.

891 **Li, Q. Y., Newbury-Ecob, R. A., Terrett, J. A., Wilson, D. I., Curtis, A. R., Yi, C. H., Gebuhr,**
892 **T., Bullen, P. J., Robson, S. C., Strachan, T., et al.** (1997). Holt-Oram syndrome is caused
893 by mutations in TBX5, a member of the Brachyury (T) gene family. *Nat Genet* **15**, 21–29.

894 **Lin, Z., Guo, H., Cao, Y., Zohrabian, S., Zhou, P., Ma, Q., VanDusen, N., Guo, Y., Zhang, J.,**
895 **Stevens, S. M., et al.** (2016). Acetylation of VGLL4 Regulates Hippo-YAP Signaling and
896 Postnatal Cardiac Growth. *Dev. Cell* **39**, 466–479.

897 **Ma, J.-F., Yang, F., Mahida, S. N., Zhao, L., Chen, X., Zhang, M. L., Sun, Z., Yao, Y., Zhang,**
898 **Y.-X., Zheng, G.-Y., et al.** (2016). TBX5 mutations contribute to early-onset atrial fibrillation
899 in Chinese and Caucasians. *Cardiovasc Res* **109**, 442–450.

900 **Man, J. C. K., Duijvenboden, K. van, Krijger, P. H. L., Hooijkaas, I. B., Made, I. van der,**
901 **Vries, C. D. G.-D., Wakker, V., Creemers, E. E., Laat, W. de, Boukens, B. J., et al.** (2021).
902 Genetic Dissection of a Super Enhancer Controlling the Nppa-NppbCluster in the Heart. *Circ*
903 *Res* **128**, 115–129.

904 **Matsson, H., Eason, J., Bookwalter, C. S., Klar, J., Gustavsson, P., Sunnegårdh, J., Enell,**
905 **H., Jonzon, A., Vikkula, M., Gutierrez, I., et al.** (2008). Alpha-cardiac actin mutations
906 produce atrial septal defects. *Hum. Mol. Genet.* **17**, 256–265.

907 **McElhinney, D. B., Krantz, I. D., Bason, L., Piccoli, D. A., Emerick, K. M., Spinner, N. B.**
908 **and Goldmuntz, E.** (2002). Analysis of Cardiovascular Phenotype and Genotype-Phenotype
909 Correlation in Individuals With a JAG1 Mutation and/or Alagille Syndrome. *Circulation* **106**,
910 2567–2574.

911 **Medrano, J. L. and Naya, F. J.** (2017). The transcription factor MEF2A fine-tunes gene
912 expression in the atrial and ventricular chambers of the adult heart. *J Biol Chem* **292**, 20975–
913 20988.

914 **Miguel, I. M. de and Ávila, P.** (2021). Atrial Fibrillation in Congenital Heart Disease. *European*
915 *Cardiol Rev* **16**, e06.

916 **Miyaoka, Y., Chan, A. H., Judge, L. M., Yoo, J., Huang, M., Nguyen, T. D., Lizarraga, P. P.,**
917 **So, P.-L. and Conklin, B. R.** (2014). Isolation of single-base genome-edited human iPS
918 cells without antibiotic selection. *Nat Meth* **11**, 291–293.

919 **Nadadur, R. D., Broman, M. T., Boukens, B., Mazurek, S. R., Yang, X., Boogaard, M. van**
920 **den, Bekeny, J., Gadek, M., Ward, T., Zhang, M., et al.** (2016). Pitx2 modulates a Tbx5-
921 dependent gene regulatory network to maintain atrial rhythm. *Science Translational Medicine*
922 **8**, 354ra115-354ra115.

923 **Nadeau, M., Georges, R. O., Laforest, B., Yamak, A., Lefebvre, C., Beauregard, J., Paradis,**
924 **P., Bruneau, B. G., Andelfinger, G. and Nemer, M.** (2010). An endocardial pathway
925 involving Tbx5, Gata4, and Nos3 required for atrial septum formation. *Proceedings of the*
926 *National Academy of Sciences* **107**, 19356–19361.

927 **Nakashima, H., Tsujimura, K., Irie, K., Ishizu, M., Pan, M., Kameda, T. and Nakashima, K.**
928 (2018). Canonical TGF-β Signaling Negatively Regulates Neuronal Morphogenesis through
929 TGIF/Smad Complex-Mediated CRMP2 Suppression. *J Neurosci* **38**, 4791–4810.

930 **Naya, F. J., Black, B. L., Wu, H., Bassel-Duby, R., Richardson, J. A., Hill, J. A. and Olson,**
931 **E. N.** (2002). Mitochondrial deficiency and cardiac sudden death in mice lacking the MEF2A
932 transcription factor. *Nat. Med.* **8**, 1303–1309.

933 **Nerbonne, J. M. and Kass, R. S.** (2005). Molecular Physiology of Cardiac Repolarization.
934 *Physiol. Rev.* **85**, 1205–1253.

935 **Olson, T. M., Alekseev, A. E., Liu, X. K., Park, S., Zingman, L. V., Bienengraeber, M.,**
936 **Sattiraju, S., Ballew, J. D., Jahangir, A. and Terzic, A.** (2006). Kv1.5 channelopathy due to
937 KCNA5 loss-of-function mutation causes human atrial fibrillation. *Hum Mol Genet* **15**, 2185–
938 2191.

939 **Ouwerkerk, A. F., Bosada, F. M., Duijvenboden, K., Hill, M. C., Montefiori, L. E., Scholman,**
940 **K. T., Liu, J., Vries, A. A. F., Boukens, B. J., Ellinor, P. T., et al.** (2019). Identification of
941 atrial fibrillation associated genes and functional non-coding variants. *Nat Commun* **10**, 1–14.

942 **Ouwerkerk, A. F. van, Bosada, F. M., Liu, J., Zhang, J., Duijvenboden, K. van, Chaffin, M.,**
943 **Tucker, N. R., Pijnappels, D., Ellinor, P. T., Barnett, P., et al.** (2020). Identification of
944 Functional Variant Enhancers Associated With Atrial Fibrillation. *Circ. Res.* **127**, 229–243.

945 **Ouwerkerk, A. F. van, Bosada, F. M., Duijvenboden, K. van, Houweling, A. C., Scholman,**
946 **K. T., Wakker, V., Allaart, C. P., Uhm, J.-S., Mathijssen, I. B., Baartscheer, T., et al.**
947 (2021). Patient-specific TBX5-G125R Variant Induces Profound Transcriptional Deregulation
948 and Atrial Dysfunction. *Circulation* **145**, 606–619.

949 **Perrone, G., Unpingco, J. and Lu, H.** (2020). Network visualizations with Pyvis and VisJS.
950 *arXiv*.

951 **Piccoli, M.-T., Gupta, S. K., Viereck, J., Foinquinos, A., Samolovac, S., Kramer, F. L., Garg,**
952 **A., Remke, J., Zimmer, K., Batkai, S., et al.** (2017). Inhibition of the Cardiac Fibroblast–
953 Enriched lncRNA Meg3 Prevents Cardiac Fibrosis and Diastolic Dysfunction. *Circ. Res.* **121**,
954 575–583.

955 **Platonov, P. G.** (2017). Atrial fibrosis: an obligatory component of arrhythmia mechanisms in
956 atrial fibrillation? *J. Geriatr. Cardiol. : JGC* **14**, 233–237.

957 **Posch, M. G., Gramlich, M., Sunde, M., Schmitt, K. R., Lee, S. H. Y., Richter, S., Kersten,**
958 **A., Perrot, A., Panek, A. N., Khatib, I. H. A., et al.** (2010). A gain-of-function TBX20
959 mutation causes congenital atrial septal defects, patent foramen ovale and cardiac valve
960 defects. *J Med Genet* **47**, 230–235.

961 **Postma, A. V., Meerakker, J. B. A. van de, Mathijssen, I. B., Barnett, P., Christoffels, V. M.,**
962 **Ilgun, A., Lam, J., Wilde, A. A. M., Deprez, R. H. L. and Moorman, A. F. M.** (2008). A gain-
963 of-function TBX5 mutation is associated with atypical Holt-Oram syndrome and paroxysmal
964 atrial fibrillation. *Circ Res* **102**, 1433–1442.

965 **Postma, A. V., Engelen, K. van, Meerakker, J. van de, Rahman, T., Probst, S., Baars, M. J.**
966 **H., Bauer, U., Pickardt, T., Sperling, S. R., Berger, F., et al.** (2011). Mutations in the
967 Sarcomere Gene MYH7 in Ebstein Anomaly. *Circ.: Cardiovasc. Genet.* **4**, 43–50.

968 **Roselli, C., Chaffin, M. D., Weng, L.-C., Aeschbacher, S., Ahlberg, G., Albert, C. M.,**
969 **Almgren, P., Alonso, A., Anderson, C. D., Aragam, K. G., et al.** (2018). Multi-ethnic
970 genome-wide association study for atrial fibrillation. *Nat Genet* 1–15.

971 **Schott, J. J., Benson, D. W., Basson, C. T., Pease, W., Silberbach, G. M., Moak, J. P.,**
972 **Maron, B. J., Seidman, C. E. and Seidman, J. G.** (1998). Congenital heart disease caused
973 by mutations in the transcription factor NKX2-5. *Science* **281**, 108–111.

974 **Seeger, T., Shrestha, R., Lam, C. K., Chen, C., McKeithan, W. L., Lau, E., Wnorowski, A.,**
975 **McMullen, G., Greenhaw, M., Lee, J., et al.** (2019). A Premature Termination Codon
976 Mutation in MYBPC3 Causes Hypertrophic Cardiomyopathy via Chronic Activation of
977 Nonsense-Mediated Decay. *Circulation* **139**, 799–811.

978 **Shafaattalab, S., Lin, E., Christidi, E., Huang, H., Nartiss, Y., Garcia, A., Lee, J., Protze, S.,**
979 **Keller, G., Brunham, L., et al.** (2019). Ibrutinib Displays Atrial-Specific Toxicity in Human
980 Stem Cell-Derived Cardiomyocytes. *Stem Cell Rep* **12**, 996–1006.

981 **Sinnecker, D., Goedel, A., Laugwitz, K.-L. and Moretti, A.** (2013). Induced Pluripotent Stem
982 Cell-Derived Cardiomyocytes. *Circ. Res.* **112**, 961–968.

983 **Smith, J. G. W., Owen, T., Bhagwan, J. R., Mosqueira, D., Scott, E., Mannhardt, I., Patel,**
984 **A., Barriales-Villa, R., Monserrat, L., Hansen, A., et al.** (2018). Isogenic Pairs of hiPSC-
985 CMs with Hypertrophic Cardiomyopathy/LVNC-Associated ACTC1 E99K Mutation Unveil
986 Differential Functional Deficits. *Stem Cell Rep.* **11**, 1226–1243.

987 **Sun, N., Yazawa, M., Liu, J., Han, L., Sanchez-Freire, V., Abilez, O. J., Navarrete, E. G., Hu,**
988 **S., Wang, L., Lee, A., et al.** (2012). Patient-Specific Induced Pluripotent Stem Cells as a
989 Model for Familial Dilated Cardiomyopathy. *Science Translational Medicine* **4**, 130ra47-
990 130ra47.

991 **Sweat, M. E., Cao, Y., Zhang, X., Burnicka-Turek, O., Perez-Cervantes, C., Kulandaisamy,**
992 **A., Lu, F., Keating, E. M., Akerberg, B. N., Ma, Q., et al.** (2023). Tbx5 maintains atrial
993 identity in postnatal cardiomyocytes by regulating an atrial-specific enhancer network. *Nat.*
994 *Cardiovasc. Res.* **2**, 881–898.

995 **Theodoris, C. V., Zhou, P., Liu, L., Zhang, Y., Nishino, T., Huang, Y., Kostina, A., Ranade,**
996 **S. S., Gifford, C. A., Uspenskiy, V., et al.** (2020). Network-based screen in iPSC-derived
997 cells reveals therapeutic candidate for heart valve disease. *Science* **371**, eabd0724-14.

998 **Turki, S. A., Manickaraj, A. K., Mercer, C. L., Gerety, S. S., Hitz, M.-P., Lindsay, S.,**
999 **D'Alessandro, L. C. A., Swaminathan, G. J., Bentham, J., Arndt, A.-K., et al.** (2014).
1000 Rare Variants in NR2F2 Cause Congenital Heart Defects in Humans. *Am. J. Hum. Genet.*
1001 **94**, 574–585.

1002 **Vad, O. B., Paludan-Muller, C., Ahlberg, G., Andreasen, L., Refsgaard, L., Lundegaard, P.**
1003 **R., Haunso, S., Svendsen, J. H. and Olesen, M. S.** (2020). Rare coding variants in MYH6
1004 are associated with atrial fibrillation: results from 45,596 exomes representing the general
1005 population. *Eur. Hear. J.* **41**, ehaa946.0342.

1006 **Xia, M., Jin, Q., Bendahhou, S., He, Y., Larroque, M.-M., Chen, Y., Zhou, Q., Yang, Y., Liu,**
1007 **Y., Liu, B., et al.** (2005). A Kir2.1 gain-of-function mutation underlies familial atrial fibrillation.
1008 *Biochem Bioph Res Co* **332**, 1012–1019.

1009 **Xie, L., Hoffmann, A. D., Burnicka-Turek, O., Friedland-Little, J. M., Zhang, K. and**
1010 **Moskowitz, I. P.** (2012). Tbx5-Hedgehog Molecular Networks Are Essential in the Second
1011 Heart Field for Atrial Septation. *Dev Cell* **23**, 280–291.

1012 **Xie, W.-H., Chang, C., Xu, Y.-J., Li, R.-G., Qu, X.-K., Fang, W.-Y., Liu, X. and Yang, Y.-Q.**
1013 (2013). Prevalence and spectrum of Nkx2.5 mutations associated with idiopathic atrial
1014 fibrillation. *Clinics* **68**, 777–784.

1015 **Yang, Y., Xia, M., Jin, Q., Bendahhou, S., Shi, J., Chen, Y., Liang, B., Lin, J., Liu, Y., Liu,**
1016 **B., et al.** (2004). Identification of a KCNE2 Gain-of-Function Mutation in Patients with
1017 Familial Atrial Fibrillation. *Am J Hum Genetics* **75**, 899–905.

1018 **Yang, X. H., Nadadur, R. D., Hilvering, C. R., Bianchi, V., Werner, M., Mazurek, S. R.,**
1019 **Gadek, M., Shen, K. M., Goldman, J. A., Tyan, L., et al.** (2017). Transcription-factor-
1020 dependent enhancer transcription defines a gene regulatory network for cardiac rhythm.
1021 *eLife* **6**, 1765.

1022 **Yang, A., Alankarage, D., Cuny, H., Ip, E. K. K., Almog, M., Lu, J., Das, D., Enriquez, A.,**
1023 **Szot, J. O., Humphreys, D. T., et al.** (2022). CHDgene: A Curated Database for Congenital
1024 Heart Disease Genes. *Circ.: Genom. Precis. Med.* **15**, e003539.

1025 **Yuan, F., Zhao, L., Wang, J., Zhang, W., Li, X., Qiu, X.-B., Li, R.-G., Xu, Y.-J., Xu, L., Qu, X.-**
1026 **K., et al.** (2013). PITX2c Loss-of-Function Mutations Responsible for Congenital Atrial Septal
1027 Defects. *Int. J. Méd. Sci.* **10**, 1422–1429.

1028 **Zhang, J. Z., Termglinchan, V., Shao, N.-Y., Itzhaki, I., Liu, C., Ma, N., Tian, L., Wang, V. Y.,**
1029 **Chang, A. C. Y., Guo, H., et al.** (2019). A Human iPSC Double-Reporter System Enables
1030 Purification of Cardiac Lineage Subpopulations with Distinct Function and Drug Response
1031 Profiles. *Cell Stem Cell* **24**, 802-811.e5.

1032

1033

Figure 1

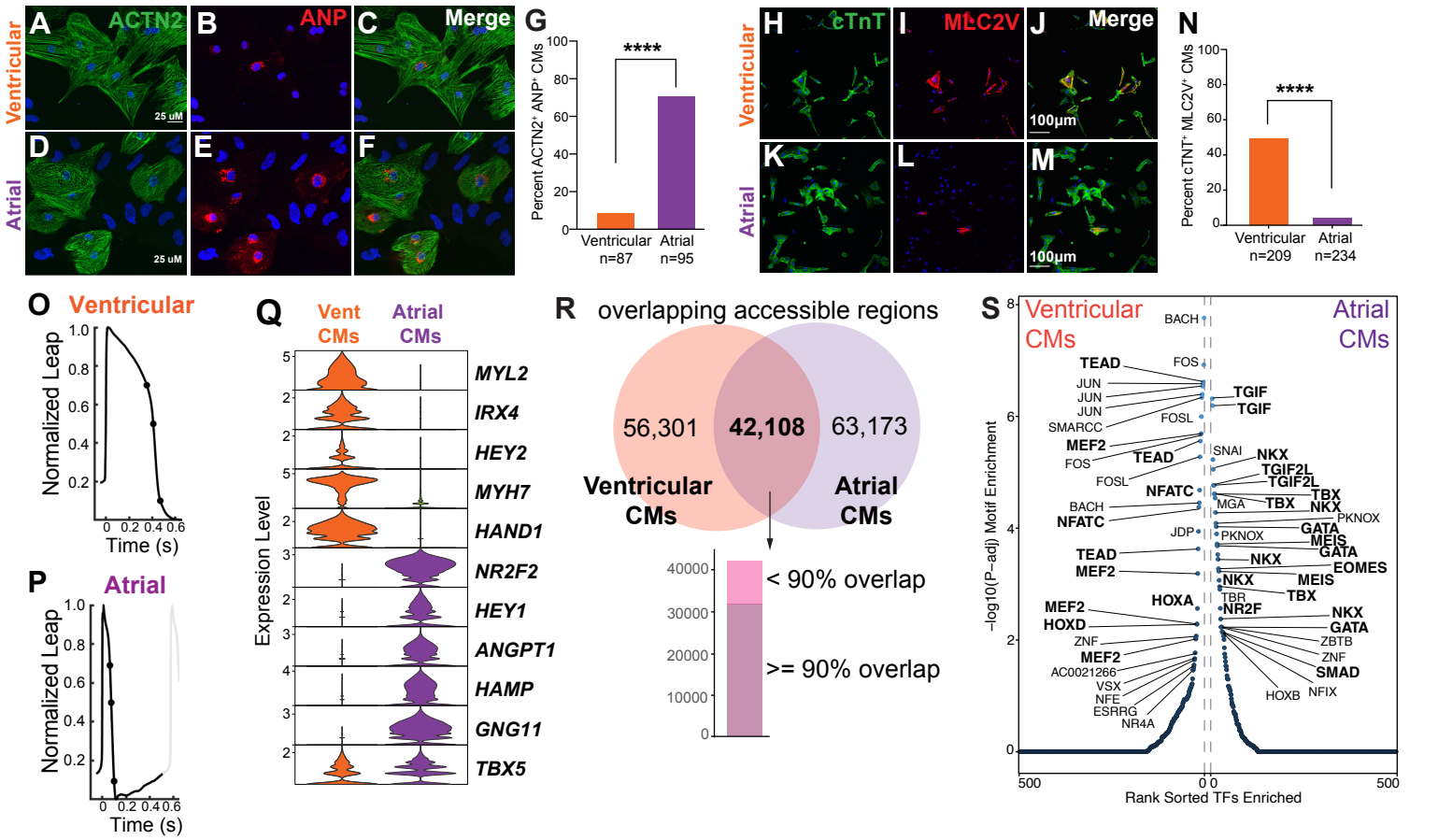
A ACTN2
B ANP
C Merge
D
E
F
Ventricular
Atrial
25 uM
G
Percent ACTN2+ ANP+ CMs
****
Ventricular n=87
Atrial n=95
H cTnT
I MLC2V
J Merge
K
L
M
100µm
N
Percent cTNT+ MLC2V+ CMs
Ventricular n=209
Atrial n=234
O Ventricular
Normalized Leap
Time (s)
P Atrial
Q Vent CMs
Atrial CMs
Expression Level
MYL2
IRX4
HEY2
MYH7
HAND1
NR2F2
HEY1
ANGPT1
HAMP
GNG11
TBX5
R overlapping accessible regions
56,301
42,108
63,173
Ventricular CMs
Atrial CMs
< 90% overlap
>= 90% overlap
S Ventricular CMs
Atrial CMs
−log10(P−adj) Motif Enrichment
Rank Sorted TFs Enriched
BACH
TEAD
FOS
JUN
SMARCC
MEF2
FOSL
SNAI
NKX
TGIF2L
NFATC
TBX
MGA
PKNOX
GATA
MEIS
JDP
EOMES
TBR
HOXA
NR2F
HOXD
ZNF
ZBTB
SMAD
AC0021266
VSX
NFE
ESRRG
NR4A
HOXB
NFIX
T Ventricular CMs
GATA4
HEY2
NKX2-5
HEY1
TBX5
E2F1
MEF2C
IRX4
HES4
HAND1
MEIS2
V Ventricular CMs
TBX5
ATP5MG
BMP5
NPPA
RBIS
CAPN3
KIFAP3
SLC8A1
TMED10
SF3B1
PNISR
KDELR1
PSMB7
CNBP
GNG5
SKP1
CYBA
TXN
PPIA
CHCHD10
SORBS2
ATP5MD
SELENOW
PAM
PPIC
PGAM1
X CMEs
WT atrial differentiation
Atrial CMs
AV CMs
Vent-like CMs
U Atrial CMs
NKX2-5
HEY2
NR2F1
TBX5
HEY1
NR2F2
HES4
PLAGL1
IRX4
MEF2C
MEIS2
HAND1
W Atrial CMs
TBX5
Y CMEs
predicted TBX5 loss
Atrial CMs
AV CMs
Vent-like CMs

Supplementary Figure 1

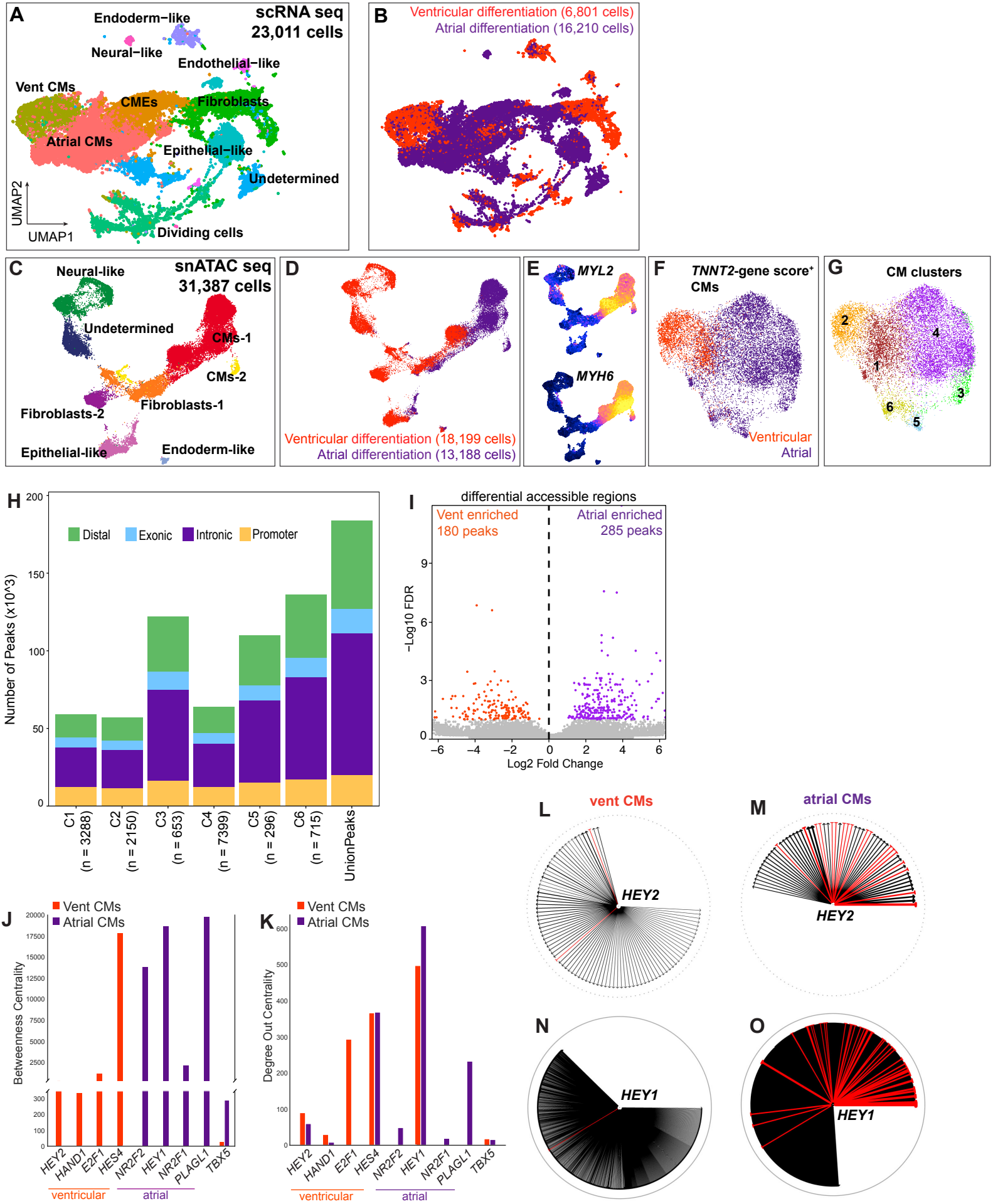

Supplementary Figure 2

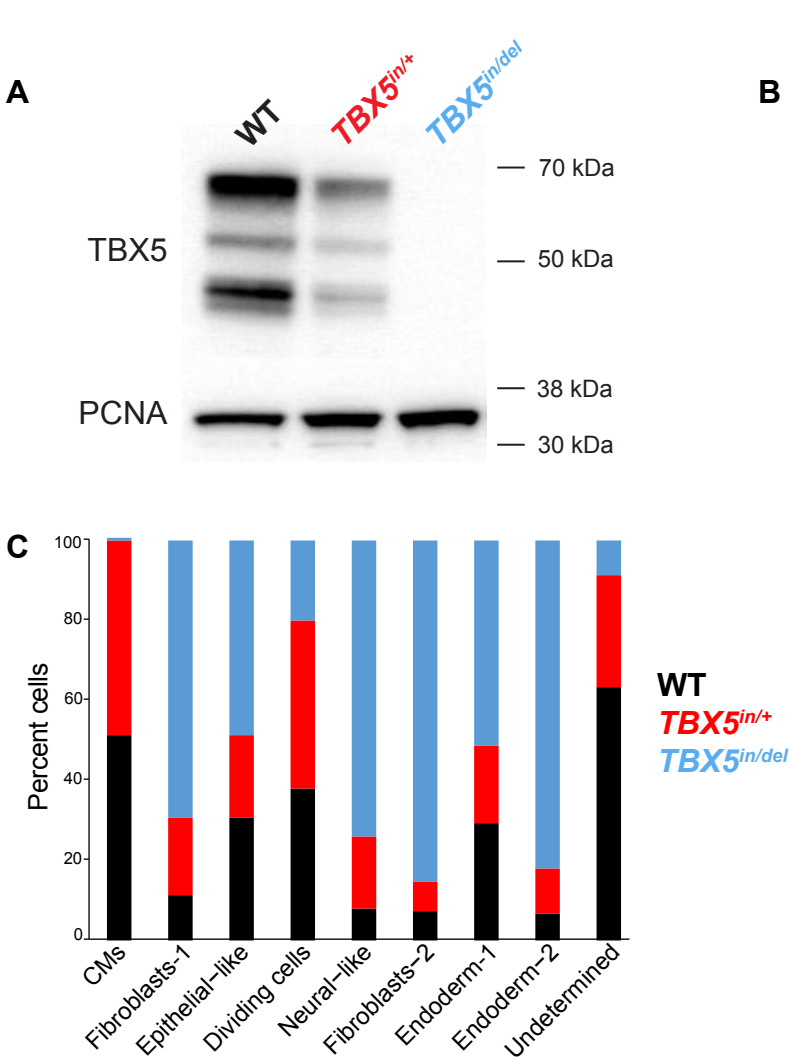

Figure 2

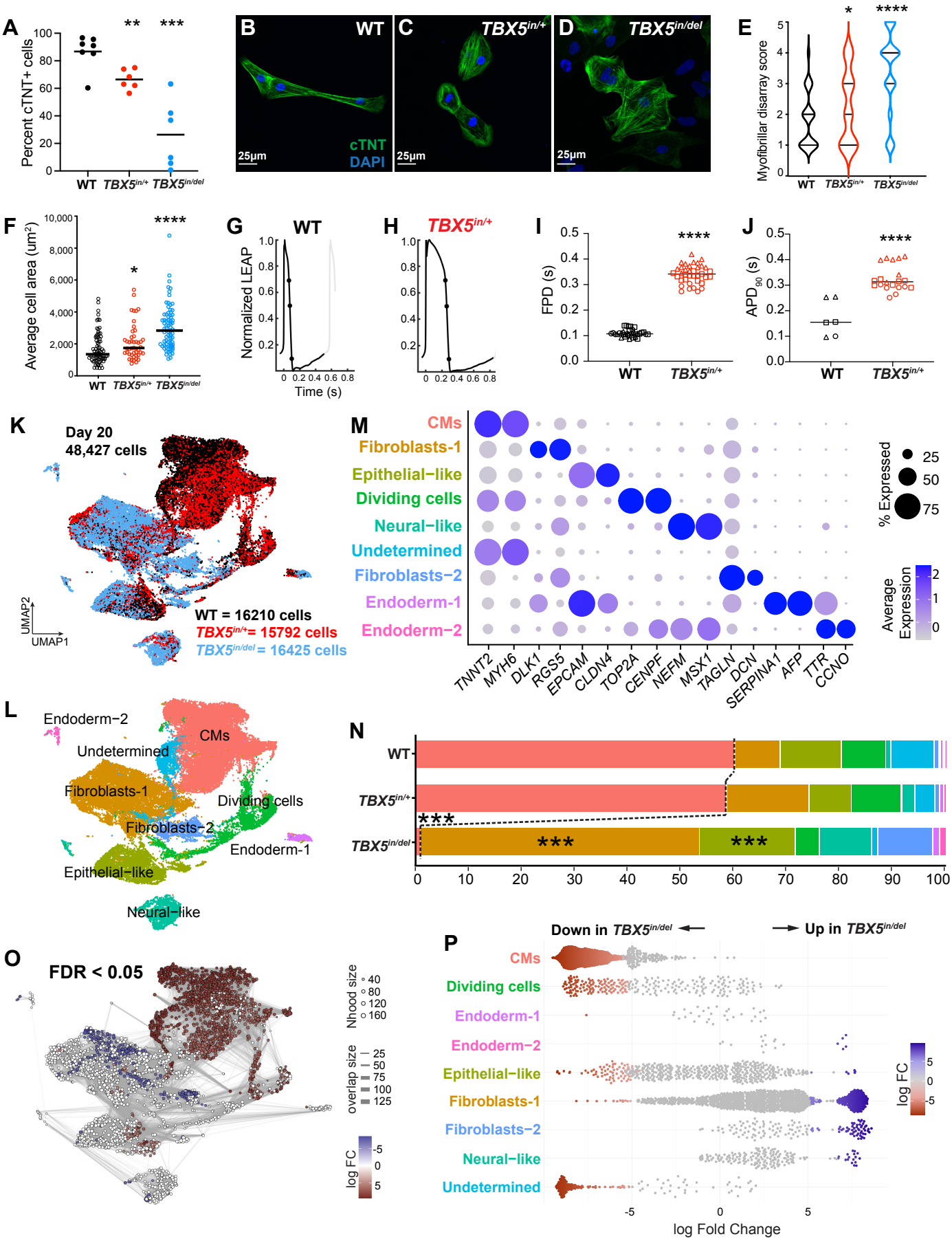
A
Percent cTNT+ cells
WT
TBX5in/+
TBX5in/del
B WT
C TBX5in/+
D TBX5in/del
cTNT
DAPI
25µm
E
Myofibrillar disarray score
F
Average cell area (um²)
G WT
H TBX5in/+
Normalized LEAP
Time (s)
I
FPD (s)
J
APD90 (s)
K
Day 20
48,427 cells
UMAP2
UMAP1
WT = 16210 cells
TBX5in/+= 15792 cells
TBX5in/del = 16425 cells
M
CMs
Fibroblasts-1
Epithelial−like
Dividing cells
Neural−like
Undetermined
Fibroblasts−2
Endoderm-1
Endoderm−2
TNNT2
MYH6
DLK1
RGS5
EPCAM
CLDN4
TOP2A
CENPF
NEFM
MSX1
TAGLN
DCN
SERPINA1
AFP
TTR
CCNO
% Expressed
Average Expression
L
Endoderm−2
CMs
Undetermined
Fibroblasts-1
Dividing cells
Fibroblasts−2
Endoderm-1
Epithelial−like
Neural−like
N
WT
TBX5in/+
TBX5in/del
O
FDR < 0.05
Nhood size
overlap size
log FC
P
Down in TBX5in/del
Up in TBX5in/del
CMs
Dividing cells
Endoderm-1
Endoderm−2
Epithelial−like
Fibroblasts-1
Fibroblasts−2
Neural−like
Undetermined
log FC
log Fold Change

Figure 3

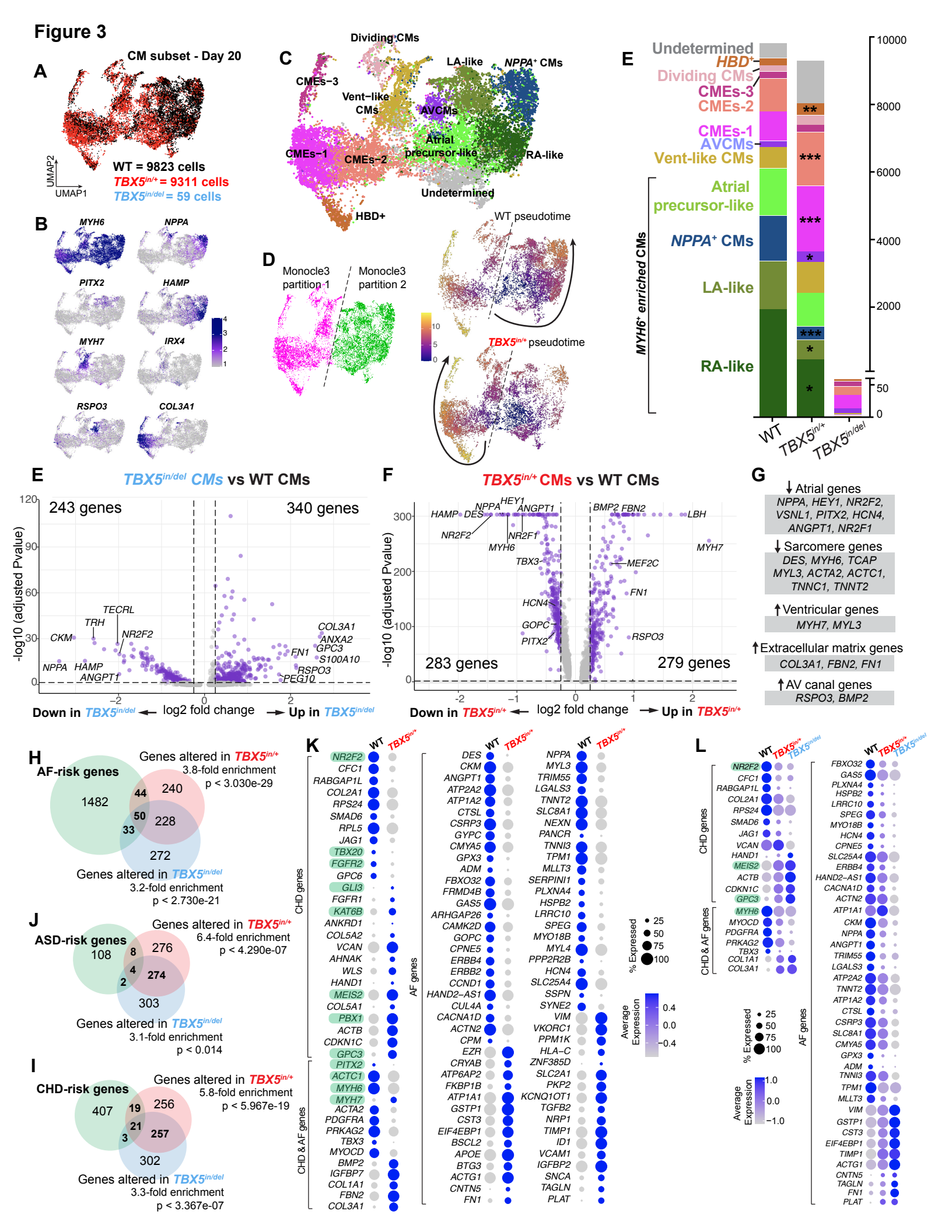
A
CM subset - Day 20
UMAP2
UMAP1
WT = 9823 cells
TBX5in/+ = 9311 cells
TBX5in/del = 59 cells
B
MYH6
NPPA
PITX2
HAMP
MYH7
IRX4
RSPO3
COL3A1
C
Dividing CMs
CMEs−3
LA-like
NPPA+ CMs
Vent−like CMs
AVCMs
Atrial precursor-like
CMEs−1
CMEs−2
RA-like
Undetermined
HBD+
D
Monocle3 partition 1
Monocle3 partition 2
WT pseudotime
TBX5in/+ pseudotime
E
Undetermined
HBD+
Dividing CMs
CMEs-3
CMEs-2
CMEs-1
AVCMs
Vent-like CMs
Atrial precursor-like
NPPA+ CMs
LA-like
RA-like
MYH6+ enriched CMs
WT
TBX5in/+
TBX5in/del
E
TBX5in/del CMs vs WT CMs
243 genes
340 genes
-log10 (adjusted Pvalue)
TECRL
TRH
CKM
NR2F2
NPPA
HAMP
ANGPT1
COL3A1
ANXA2
GPC3
S100A10
FN1
RSPO3
PEG10
Down in TBX5in/del
log2 fold change
Up in TBX5in/del
F
TBX5in/+ CMs vs WT CMs
HAMP
DES
NPPA
HEY1
ANGPT1
NR2F2
NR2F1
MYH6
TBX3
HCN4
GOPC
PITX2
BMP2
FBN2
LBH
MYH7
MEF2C
FN1
RSPO3
283 genes
279 genes
Down in TBX5in/+
log2 fold change
Up in TBX5in/+
G
Atrial genes
NPPA, HEY1, NR2F2, VSNL1, PITX2, HCN4, ANGPT1, NR2F1
Sarcomere genes
DES, MYH6, TCAP MYL3, ACTA2, ACTC1, TNNC1, TNNT2
Ventricular genes
MYH7, MYL3
Extracellular matrix genes
COL3A1, FBN2, FN1
AV canal genes
RSPO3, BMP2
H
AF-risk genes
Genes altered in TBX5in/+
3.8-fold enrichment
p < 3.030e-29
1482
44
240
50
228
33
272
Genes altered in TBX5in/del
3.2-fold enrichment
p < 2.730e-21
J
ASD-risk genes
Genes altered in TBX5in/+
6.4-fold enrichment
p < 4.290e-07
108
8
276
4
274
2
303
Genes altered in TBX5in/del
3.1-fold enrichment
p < 0.014
I
CHD-risk genes
Genes altered in TBX5in/+
5.8-fold enrichment
p < 5.967e-19
407
19
256
21
257
3
302
Genes altered in TBX5in/del
3.3-fold enrichment
p < 3.367e-07
K
WT
TBX5in/+
CHD genes
NR2F2
CFC1
RABGAP1L
COL2A1
RPS24
SMAD6
RPL5
JAG1
TBX20
FGFR2
GPC6
GLI3
FGFR1
KAT6B
ANKRD1
COL5A2
VCAN
AHNAK
WLS
HAND1
MEIS2
COL5A1
PBX1
ACTB
CDKN1C
GPC3
PITX2
CHD & AF genes
ACTC1
MYH6
MYH7
ACTA2
PDGFRA
PRKAG2
TBX3
MYOCD
BMP2
IGFBP7
COL1A1
FBN2
COL3A1
AF genes
DES
CKM
ANGPT1
ATP2A2
ATP1A2
CTSL
CSRP3
GYPC
CMYA5
GPX3
ADM
FBXO32
FRMD4B
GAS5
ARHGAP26
CAMK2D
GOPC
CPNE5
ERBB4
ERBB2
CCND1
HAND2-AS1
CUL4A
CACNA1D
ACTN2
CPM
EZR
CRYAB
ATP6AP2
FKBP1B
ATP1A1
GSTP1
CST3
EIF4EBP1
BSCL2
APOE
BTG3
ACTG1
CNTN5
FN1
NPPA
MYL3
TRIM55
LGALS3
TNNT2
SLC8A1
NEXN
PANCR
TNNI3
TPM1
MLLT3
SERPINI1
PLXNA4
HSPB2
LRRC10
SPEG
MYO18B
MYL4
PPP2R2B
HCN4
SLC25A4
SSPN
SYNE2
VIM
VKORC1
PPM1K
HLA-C
ZNF385D
SLC2A1
PKP2
KCNQ1OT1
TGFB2
NRP1
TIMP1
ID1
VCAM1
IGFBP2
SNCA
TAGLN
PLAT
% Expressed
25
50
75
100
Average Expression
0.4
0.0
−0.4
L
WT
TBX5in/+
TBX5in/del
CHD genes
NR2F2
CFC1
RABGAP1L
COL2A1
RPS24
SMAD6
JAG1
VCAN
HAND1
MEIS2
ACTB
CDKN1C
GPC3
CHD & AF genes
MYH6
MYOCD
PDGFRA
PRKAG2
TBX3
COL1A1
COL3A1
AF genes
FBXO32
GAS5
PLXNA4
HSPB2
LRRC10
SPEG
MYO18B
HCN4
CPNE5
SLC25A4
ERBB4
HAND2-AS1
CACNA1D
ACTN2
ATP1A1
CKM
NPPA
ANGPT1
TRIM55
LGALS3
ATP2A2
TNNT2
ATP1A2
CTSL
CSRP3
SLC8A1
CMYA5
GPX3
ADM
TNNI3
TPM1
MLLT3
VIM
GSTP1
CST3
EIF4EBP1
TIMP1
ACTG1
CNTN5
TAGLN
FN1
PLAT
% Expressed
25
50
75
100
Average Expression
1.0
0.0
−1.0

Supplementary Figure 3

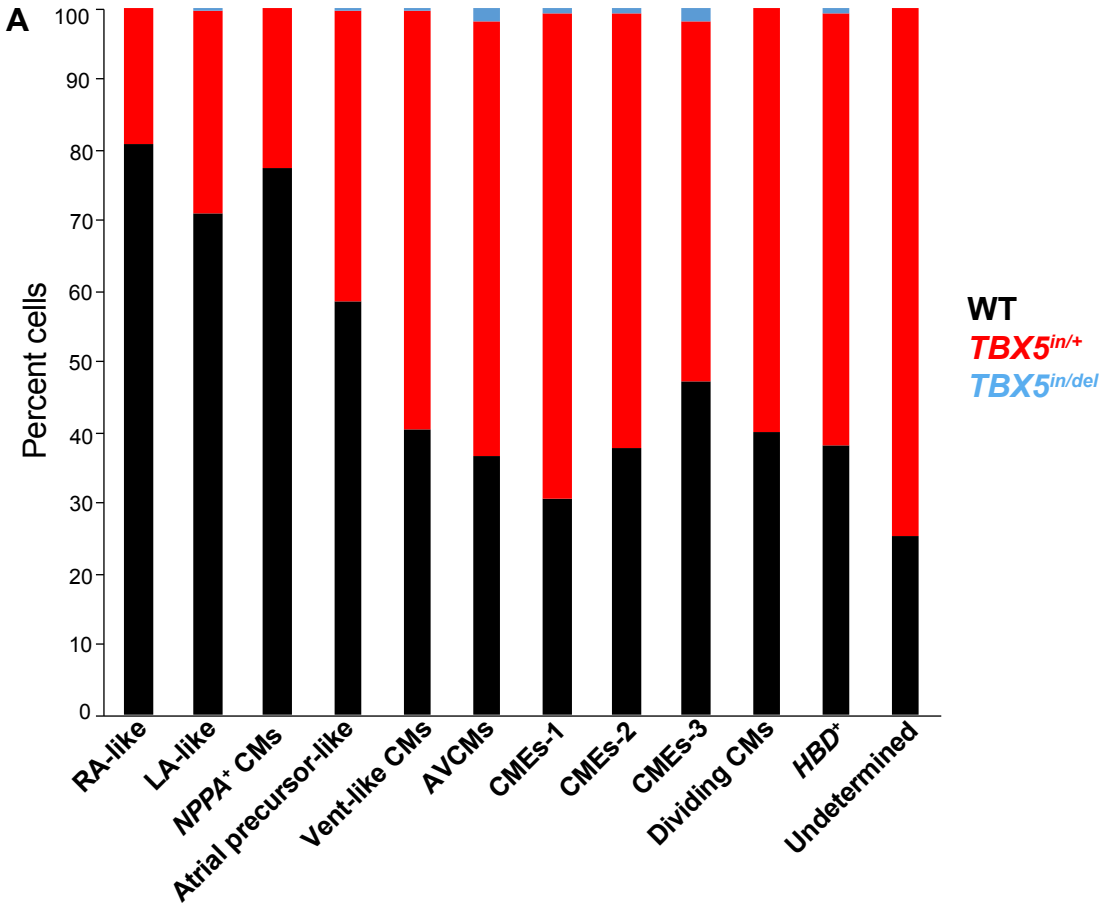

Figure 4

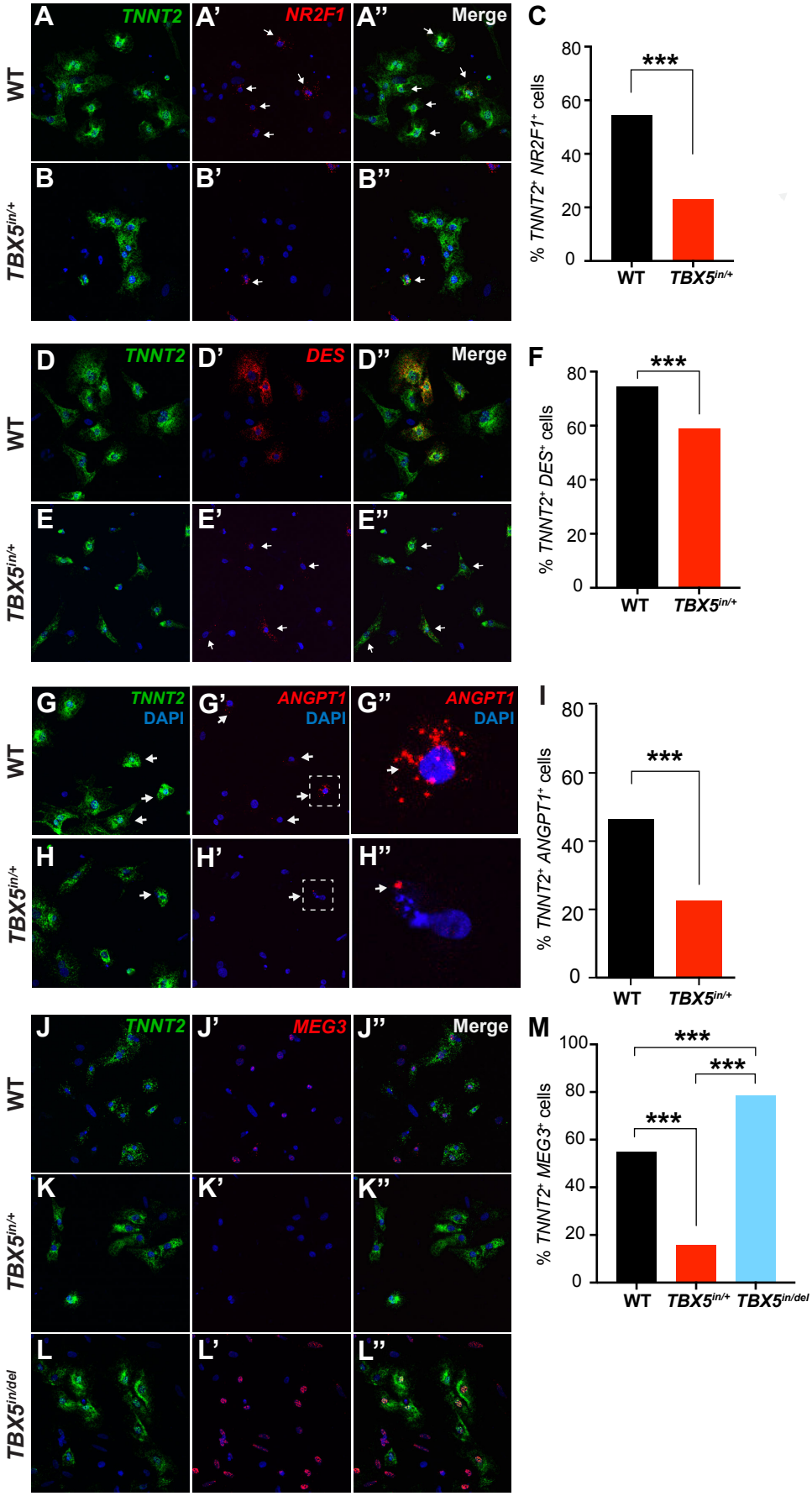
A
TNNT2
A'
NR2F1
A''
Merge
WT
B
B'
B''
TBX5in/+
C
% TNNT2+ NR2F1+ cells
***
80
60
40
20
0
WT
TBX5in/+
D
TNNT2
D'
DES
D''
Merge
WT
E
E'
E''
TBX5in/+
F
% TNNT2+ DES+ cells
***
80
60
40
20
0
WT
TBX5in/+
G
TNNT2
DAPI
G'
ANGPT1
DAPI
G''
ANGPT1
DAPI
WT
H
H'
H''
TBX5in/+
I
% TNNT2+ ANGPT1+ cells
***
80
60
40
20
0
WT
TBX5in/+
J
TNNT2
J'
MEG3
J''
Merge
WT
K
K'
K''
TBX5in/+
L
L'
L''
TBX5in/del
M
% TNNT2+ MEG3+ cells
***
***
***
100
80
60
40
20
0
WT
TBX5in/+
TBX5in/del

Fig. S4

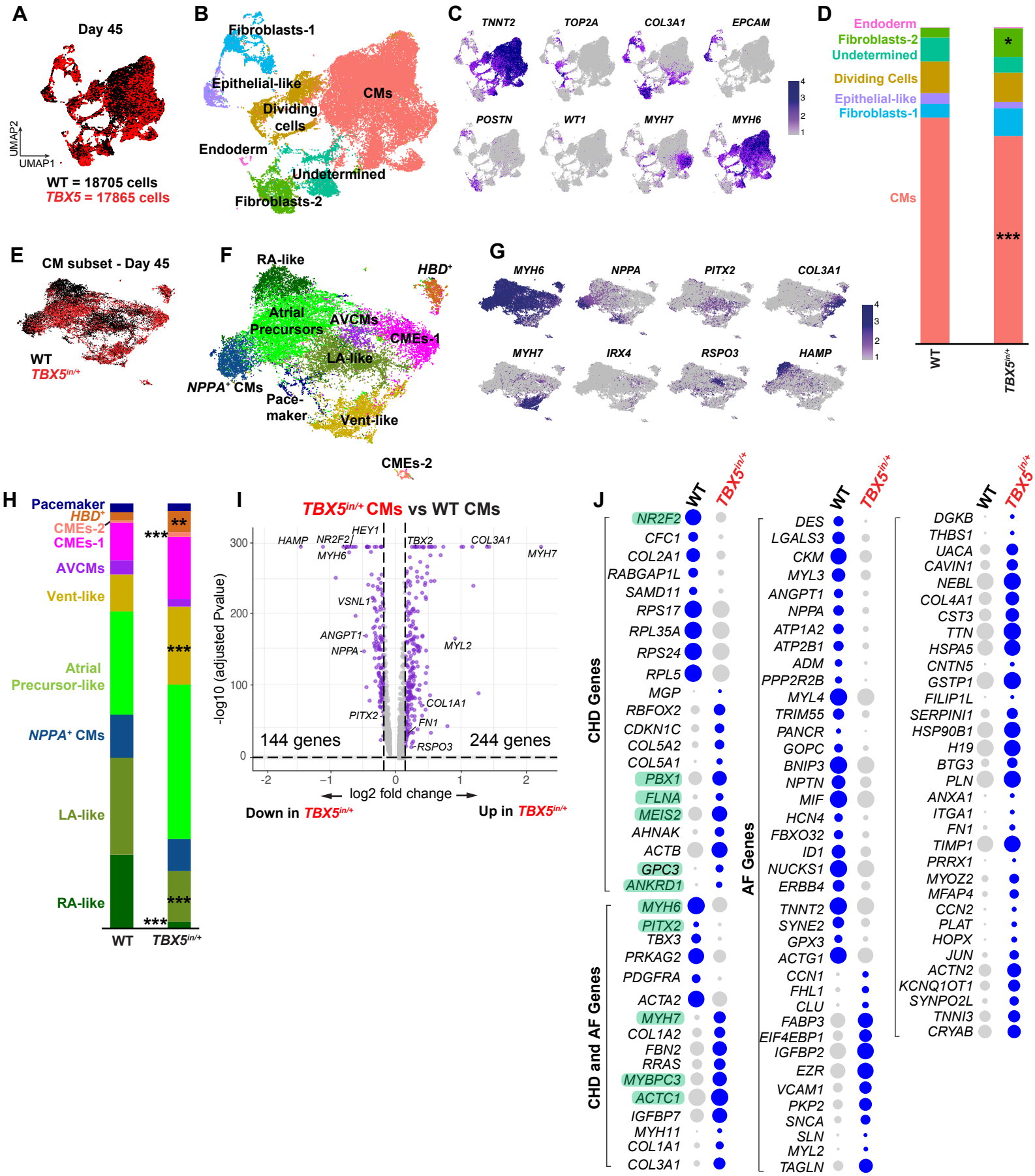
A
Day 45
UMAP2
UMAP1
WT = 18705 cells
TBX5 = 17865 cells
B
Fibroblasts-1
Epithelial-like
Dividing cells
CMs
Endoderm
Undetermined
Fibroblasts-2
C
TNNT2
TOP2A
COL3A1
EPCAM
POSTN
WT1
MYH7
MYH6
D
Endoderm
Fibroblasts-2
Undetermined
Dividing Cells
Epithelial-like
Fibroblasts-1
CMs
WT
TBX5in/+
E
CM subset - Day 45
WT
TBX5in/+
F
RA-like
HBD+
Atrial Precursors
AVCMs
CMEs-1
LA-like
NPPA+ CMs
Pace-maker
Vent-like
CMEs-2
G
MYH6
NPPA
PITX2
COL3A1
MYH7
IRX4
RSPO3
HAMP
H
Pacemaker
HBD+
CMEs-2
CMEs-1
AVCMs
Vent-like
Atrial Precursor-like
NPPA+ CMs
LA-like
RA-like
WT
TBX5in/+
I
TBX5in/+ CMs vs WT CMs
-log10 (adjusted Pvalue)
log2 fold change
144 genes
244 genes
Down in TBX5in/+
Up in TBX5in/+
HAMP
NR2F2
HEY1
MYH6
TBX2
COL3A1
MYH7
VSNL1
ANGPT1
NPPA
MYL2
COL1A1
PITX2
FN1
RSPO3
J
WT
TBX5in/+
CHD Genes
CHD and AF Genes
AF Genes
NR2F2
CFC1
COL2A1
RABGAP1L
SAMD11
RPS17
RPL35A
RPS24
RPL5
MGP
RBFOX2
CDKN1C
COL5A2
COL5A1
PBX1
FLNA
MEIS2
AHNAK
ACTB
GPC3
ANKRD1
MYH6
PITX2
TBX3
PRKAG2
PDGFRA
ACTA2
MYH7
COL1A2
FBN2
RRAS
MYBPC3
ACTC1
IGFBP7
MYH11
COL1A1
COL3A1
DES
LGALS3
CKM
MYL3
ANGPT1
NPPA
ATP1A2
ATP2B1
ADM
PPP2R2B
MYL4
TRIM55
PANCR
GOPC
BNIP3
NPTN
MIF
HCN4
FBXO32
ID1
NUCKS1
ERBB4
TNNT2
SYNE2
GPX3
ACTG1
CCN1
FHL1
CLU
FABP3
EIF4EBP1
IGFBP2
EZR
VCAM1
PKP2
SNCA
SLN
MYL2
TAGLN
DGKB
THBS1
UACA
CAVIN1
NEBL
COL4A1
CST3
TTN
HSPA5
CNTN5
GSTP1
FILIP1L
SERPINI1
HSP90B1
H19
BTG3
PLN
ANXA1
ITGA1
FN1
TIMP1
PRRX1
MYOZ2
MFAP4
CCN2
PLAT
HOPX
JUN
ACTN2
KCNQ1OT1
SYNPO2L
TNNI3
CRYAB

Fig. S5

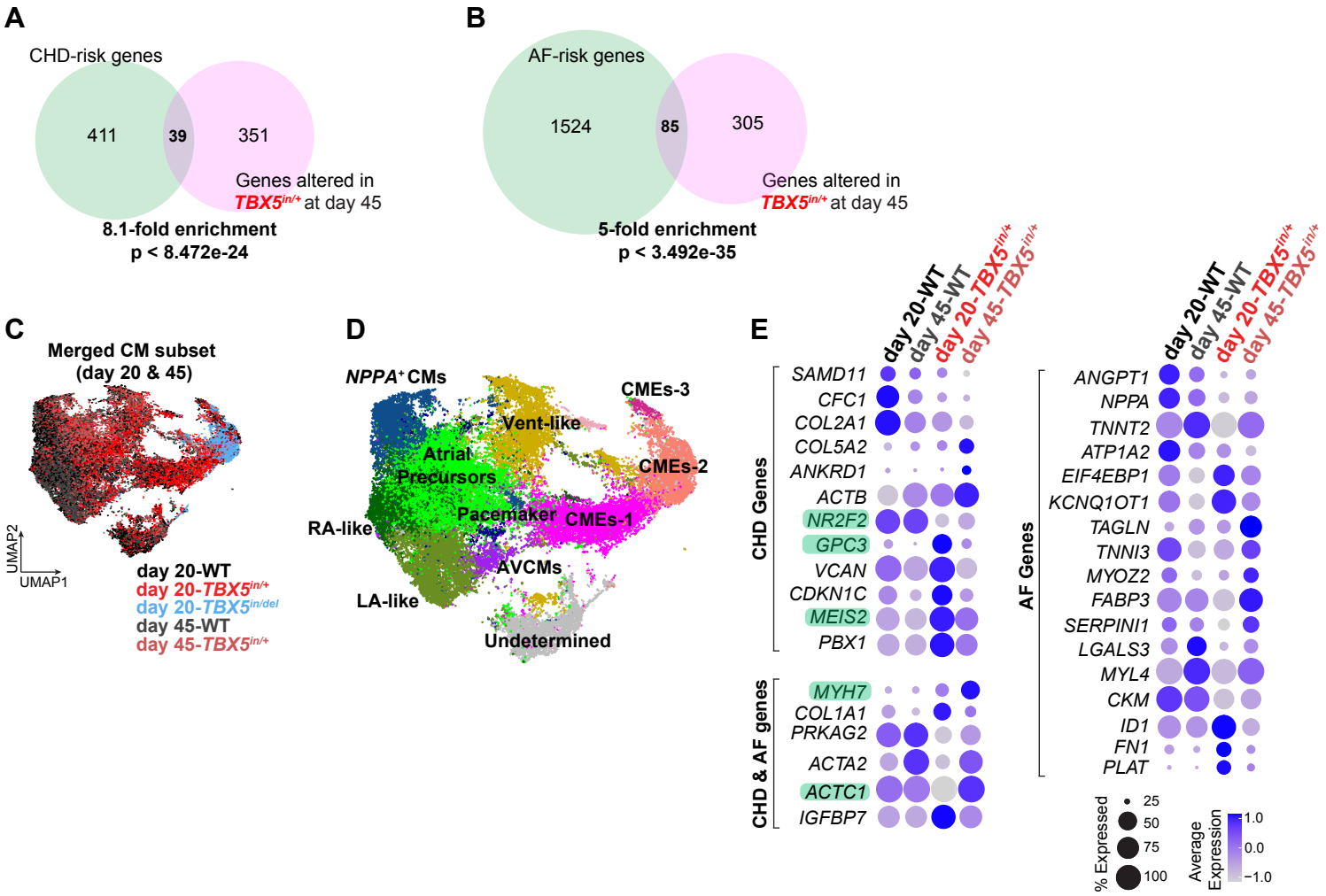
A
CHD-risk genes
411
39
351
Genes altered in
TBX5in/+ at day 45
8.1-fold enrichment
p < 8.472e-24
B
AF-risk genes
1524
85
305
Genes altered in
TBX5in/+ at day 45
5-fold enrichment
p < 3.492e-35
C
Merged CM subset
(day 20 & 45)
UMAP2
UMAP1
day 20-WT
day 20-TBX5in/+
day 20-TBX5in/del
day 45-WT
day 45-TBX5in/+
D
NPPA+ CMs
CMEs-3
Vent-like
Atrial
Precursors
CMEs-2
RA-like
Pacemaker
CMEs-1
AVCMs
LA-like
Undetermined
E
day 20-WT
day 45-WT
day 20-TBX5in/+
day 45-TBX5in/+
CHD Genes
SAMD11
CFC1
COL2A1
COL5A2
ANKRD1
ACTB
NR2F2
GPC3
VCAN
CDKN1C
MEIS2
PBX1
CHD & AF genes
MYH7
COL1A1
PRKAG2
ACTA2
ACTC1
IGFBP7
AF Genes
ANGPT1
NPPA
TNNT2
ATP1A2
EIF4EBP1
KCNQ1OT1
TAGLN
TNNI3
MYOZ2
FABP3
SERPINI1
LGALS3
MYL4
CKM
ID1
FN1
PLAT
% Expressed
25
50
75
100
Average Expression
1.0
0.0
−1.0

Figure 5

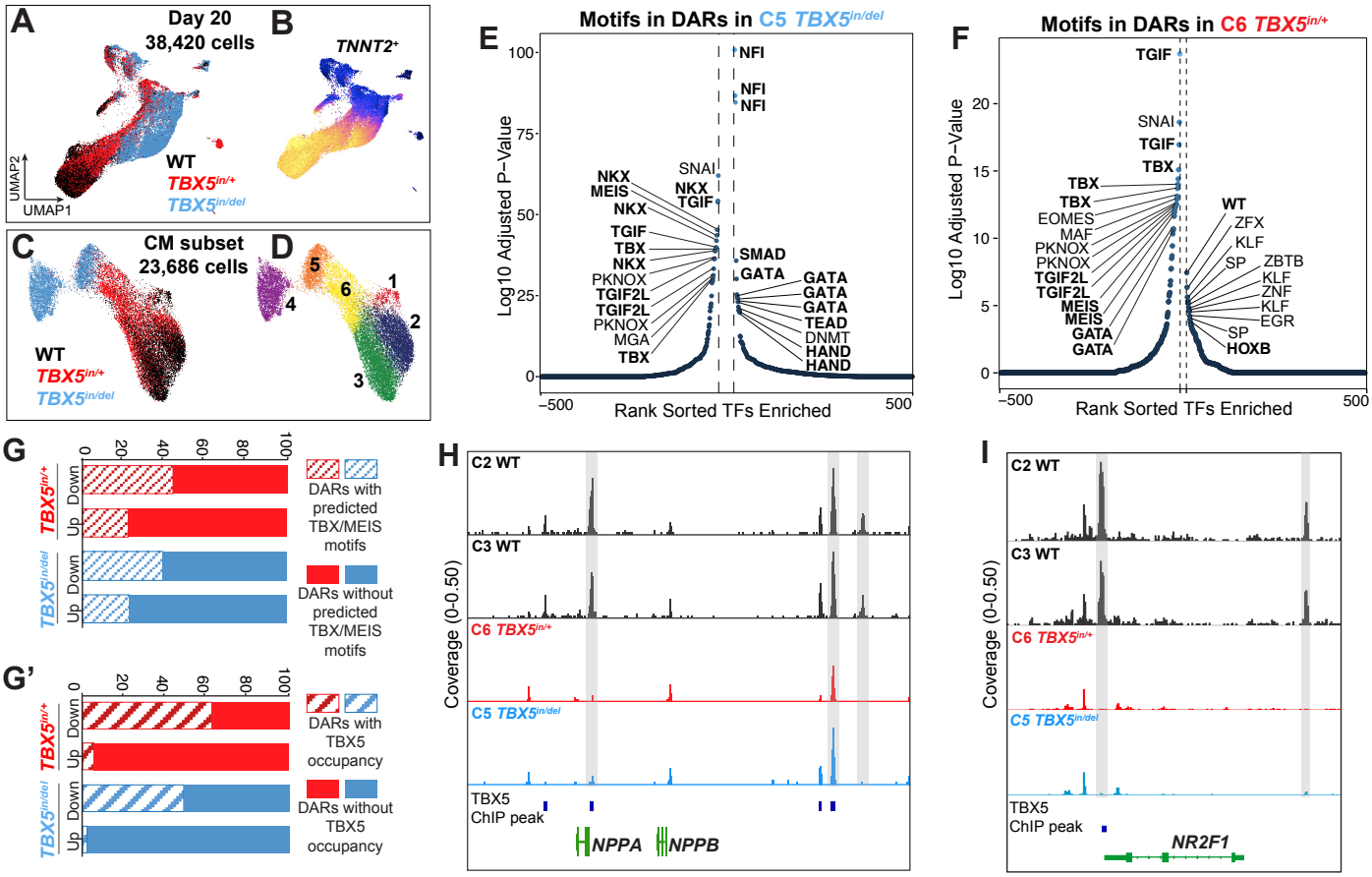
A
Day 20
38,420 cells
WT
TBX5in/+
TBX5in/del
UMAP2
UMAP1
B
TNNT2+
C
CM subset
23,686 cells
WT
TBX5in/+
TBX5in/del
D
1
2
3
4
5
6
E
Motifs in DARs in C5 TBX5in/del
Log10 Adjusted P−Value
Rank Sorted TFs Enriched
NFI
NFI
NFI
SNAI
NKX
MEIS
NKX
TGIF
NKX
TGIF
TBX
NKX
PKNOX
TGIF2L
TGIF2L
PKNOX
MGA
TBX
SMAD
GATA
GATA
GATA
GATA
GATA
TEAD
DNMT
HAND
HAND
F
Motifs in DARs in C6 TBX5in/+
Log10 Adjusted P−Value
Rank Sorted TFs Enriched
TGIF
SNAI
TGIF
TBX
TBX
TBX
EOMES
MAF
PKNOX
PKNOX
TGIF2L
TGIF2L
MEIS
MEIS
GATA
GATA
WT
ZFX
KLF
SP
ZBTB
KLF
ZNF
KLF
EGR
SP
HOXB
G
TBX5in/+
TBX5in/del
Down
Up
DARs with predicted TBX/MEIS motifs
DARs without predicted TBX/MEIS motifs
G'
DARs with TBX5 occupancy
DARs without TBX5 occupancy
H
C2 WT
C3 WT
C6 TBX5in/+
C5 TBX5in/del
Coverage (0-0.50)
TBX5 ChIP peak
NPPA
NPPB
I
C2 WT
C3 WT
C6 TBX5in/+
C5 TBX5in/del
Coverage (0-0.50)
TBX5 ChIP peak
NR2F1

Supplementary Figure 6

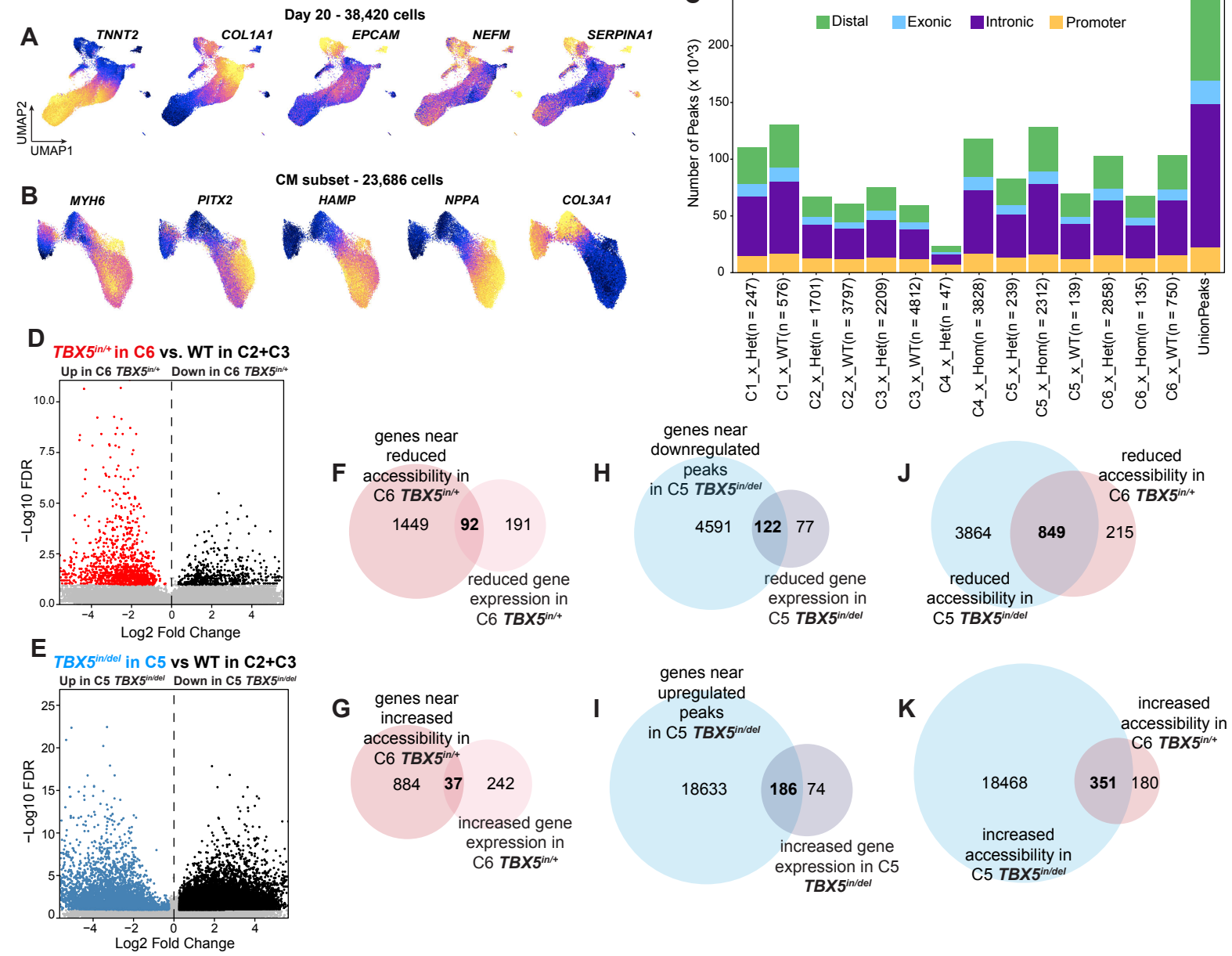

Figure 6

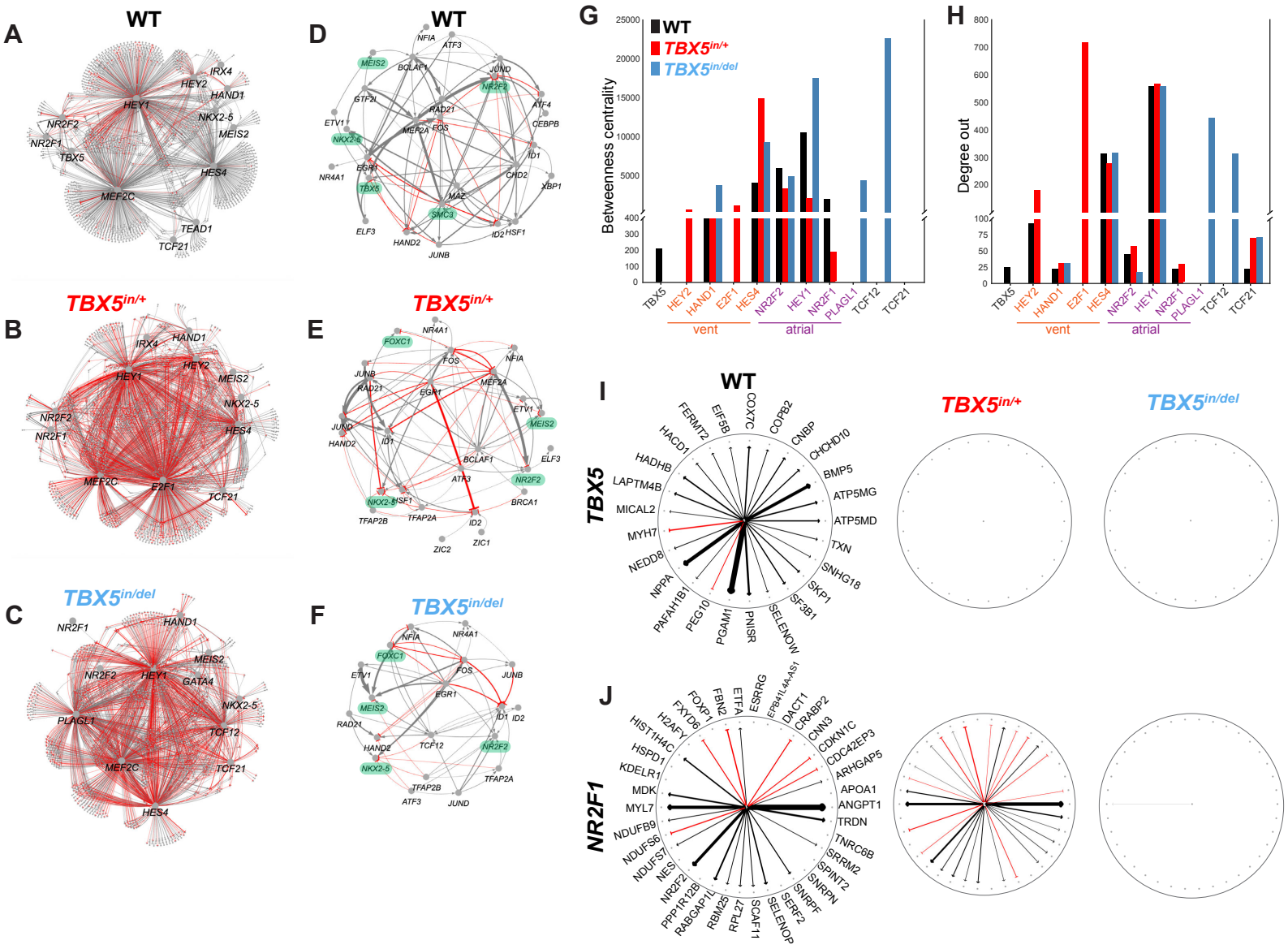
A
WT
IRX4
HEY2
HAND1
HEY1
NKX2-5
NR2F2
MEIS2
NR2F1
TBX5
HES4
MEF2C
TEAD1
TCF21
B
TBX5in/+
IRX4
HAND1
HEY2
HEY1
MEIS2
NKX2-5
NR2F2
HES4
NR2F1
MEF2C
E2F1
TCF21
C
TBX5in/del
NR2F1
HAND1
MEIS2
NR2F2
HEY1
GATA4
NKX2-5
PLAGL1
TCF12
MEF2C
TCF21
HES4
D
WT
NFIA
ATF3
MEIS2
BCLAF1
JUND
NR2F2
GTF2I
RAD21
ATF4
ETV1
MEF2A
FOS
CEBPB
NKX2-8
ID1
EGR1
CHD2
NR4A1
XBP1
TBX5
MAZ
SMC3
ELF3
ID2
HSF1
HAND2
JUNB
E
TBX5in/+
NR4A1
FOXC1
FOS
NFIA
JUNB
MEF2A
RAD21
EGR1
ETV1
MEIS2
JUND
HAND2
ID1
BCLAF1
ELF3
ATF3
NR2F2
NKX2-5
HSF1
BRCA1
TFAP2B
TFAP2A
ID2
ZIC2
ZIC1
F
TBX5in/del
NFIA
NR4A1
FOXC1
ETV1
FOS
JUNB
EGR1
MEIS2
ID1
ID2
RAD21
HAND2
TCF12
NR2F2
NKX2-5
TFAP2A
TFAP2B
ATF3
JUND
G
WT
TBX5in/+
TBX5in/del
Betweenness centrality
25000
20000
15000
10000
5000
400
300
200
100
0
TBX5
HEY2
HAND1
E2F1
HES4
NR2F2
HEY1
NR2F1
PLAGL1
TCF12
TCF21
vent
atrial
H
Degree out
800
700
600
500
400
300
200
100
75
50
25
0
TBX5
HEY2
HAND1
E2F1
HES4
NR2F2
HEY1
NR2F1
PLAGL1
TCF12
TCF21
vent
atrial
I
WT
TBX5
COX7C
COPB2
CNBP
CHCHD10
BMP5
ATP5MG
ATP5MD
TXN
SNHG18
SKP1
SF3B1
SELENOW
PNISR
PGAM1
PEG10
PAFAH1B1
NPPA
NEDD8
MYH7
MICAL2
LAPTM4B
HADHB
HACD1
FERMT2
EIF5B
TBX5in/+
TBX5in/del
J
NR2F1
ESRRG
EFB41L-AA-AS1
DACT1
CRABP2
CNN3
CDKN1C
CDC42EP3
ARHGAP5
APOA1
ANGPT1
TRDN
TNRC6B
SRRM2
SPINT2
SNRPN
SNRPF
SERF2
SELENOP
SCAF11
RPL27
RBM25
RABGAP1L
PPP1R12B
NR2F2
NES
NDUFS7
NDUFS6
NDUFB9
MYL7
MDK
KDELR1
HSPD1
HIST1H4C
H2AFY
FXYD6
FOXP1
FBN2
ETFA
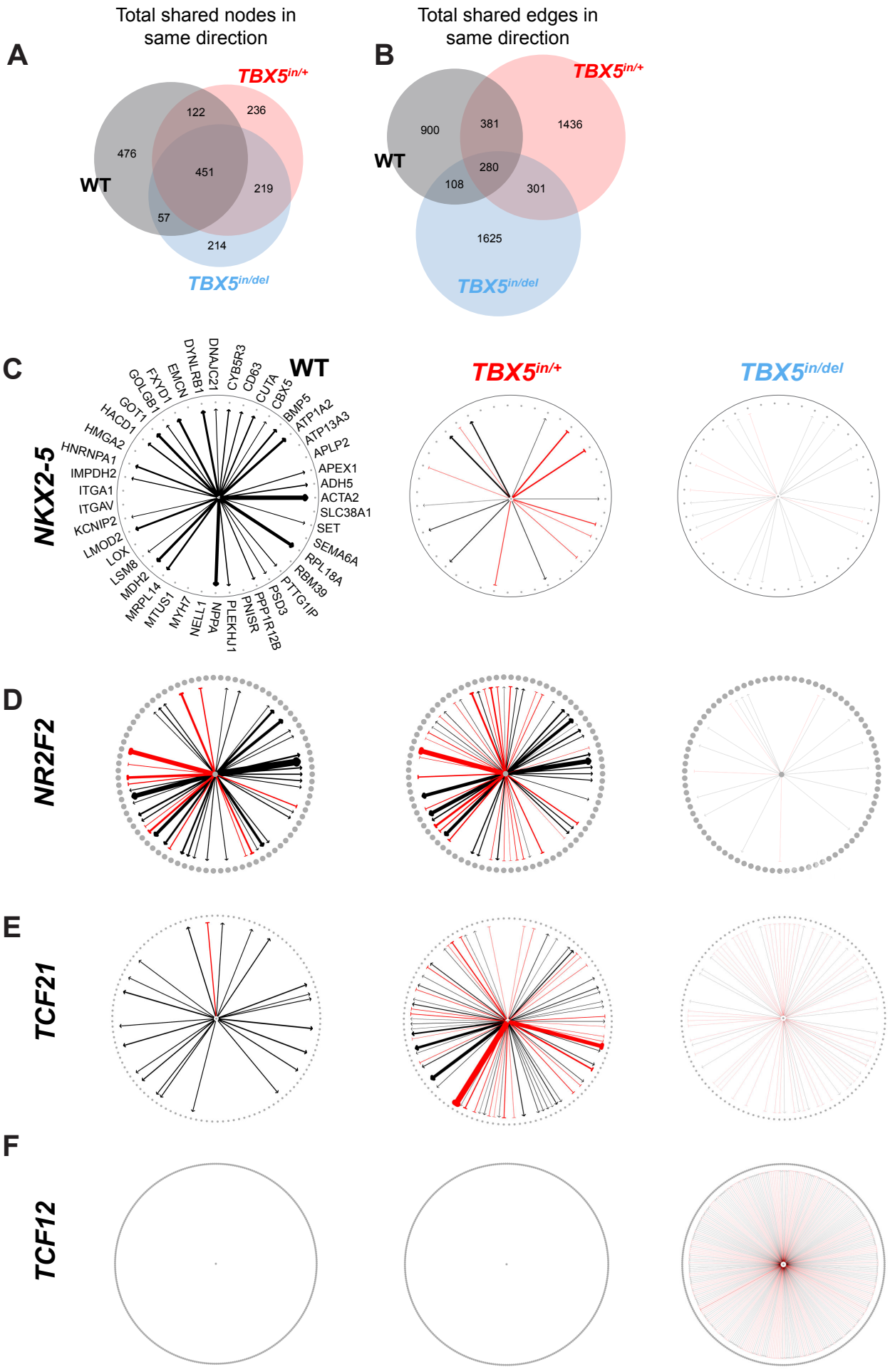
Supplementary Figure 7